

Unterschrift des Betreuers



TECHNISCHE
UNIVERSITÄT
WIEN

DIPLOMARBEIT

Vibrational Signatures in Time-resolved Electronic Spectroscopy of Hypericin

Ausgeführt am Institut für Chemische Technologien und Analytik
und am Institut für Photonik
der Technischen Universität Wien

unter der Anleitung von Univ.Ass. Dr.rer.nat. Jürgen Hauer, MSc
und Ao.Univ.Prof. Dipl.-Ing. Dr.techn. Bernhard Lendl

durch

Jakob Hayden, BSc

0928812

Prinzersdorfer Straße 9
A-3110 Neudling

Wien, am 4.1.2016

Acknowledgements / Danksagung

First and foremost I am indebted to Jürgen Hauer and Craig Lincoln who made this thesis possible in the first place. I will not forget the time and effort they put into my training without prospect of reward. Thank you!

I want to thank František Šanda for passionately and patiently teaching me the theory of nonlinear spectroscopy.

Thanks goes to Arpa Galestian Pour for her ever friendly and supportive attitude.

Ich danke Karin Wieland für die Messung resonanter Raman Spektren.

Mein aufrichtiger Dank gilt Bernhard Lendl, dafür, dass er mich in diesem, vorangegangenen und nachfolgenden Projekten unterstützt hat und unterstützt und mich in meinem Wirken stets bestärkt.

Ich danke Bettina Baumgartner für ihre Liebe, Geduld und Begleitung auf meinem Weg zu dieser Arbeit. Du hast meine Studienzeit mit viel Freude erfüllt.

Besonderer Dank gilt meinem Vater, Franz Hayden, der mich nie vergessen lässt, dass seine Liebe zu mir an keine Bedingungen geknüpft ist und der mich immer unterstützt hat.

Wertvolle und wichtige Stützen sind und waren stets meine Schwester, Judith Hayden und meine Großmütter, Josefa Frosch und Gerlinde Hayden. Danke dafür!

Abstract

Research on light induced molecular dynamical processes progressed tremendously in the last decades due to the advent of nonlinear optical spectroscopic techniques with femtosecond time resolution. In this field of research, the visible spectral regime is of outmost interest because light of visible wavelengths drives and probes electronic transitions in molecules. It can thus be used to investigate processes that start from an electronically excited state, *e.g.* visual phototransduction (the conversion of light into an electric stimulus in the eye) or photosynthesis. In spite of their electronic initiation, nuclear motion and especially such along vibrational coordinates plays a major role in these processes since all chemical reactions proceed *via* a change in nuclear arrangement. As an example, energy transfer in the initial steps of photosynthesis is mediated *via* vibrational motion. Also, as described by the Franck-Condon principle, the coupling of vibrations to electronic transitions yields significant contributions in visible spectra and is therefore essential for their interpretation. The fundamental role of molecular vibrations calls for a profound description and study of vibrational signatures in time resolved electronic spectra.

This thesis addresses such signatures as measured by heterodyned transient grating spectroscopy of the model molecule hypericin. Vibrations modulating the visible spectra are recorded in the time domain, which allows for the retrieval of both, vibrational amplitude *and* phase in their signal wavelength dependence. The resulting spectra are compared with theoretical predictions based on the universal theoretical frame work of nonlinear response theory, which is shown to be a valid and especially insightful alternative to the more common treatment in the wavepacket formalism. The methodology presented in this thesis not only readily explains experimental findings but is applicable to a much wider range of molecules than hypericin or solvated molecules in general. For example, the study of vibrational-electronic coupling in energy transfer in light harvesting complexes is a logical continuation of this work.

Kurzfassung

Die Erforschung lichtinduzierter molekulardynamischer Prozesse entwickelte sich in den vergangenen Dekaden auf Grund der Etablierung nichtlinearer spektroskopischer Methoden mit zeitlicher Auflösung im Femtosekunden - Bereich enorm weiter. In diesem Forschungsfeld kommt dem sichtbaren Spektralbereich eine besondere Rolle zu, da Licht sichtbarer Wellenlängen elektronische Übergänge in Molekülen bewirkt beziehungsweise abfragt. Er kann daher herangezogen werden, um Vorgänge zu untersuchen, die in elektronisch angeregten Zuständen beginnen. Beispiele für solche Vorgänge sind die visuelle Phototransduktion (Umwandlung von Licht in einen elektrischen Reiz im Auge) oder die Photosynthese. Trotz ihrer elektronischen Initialisierung spielen auch Bewegungen von Kernen, insbesondere solche entlang vibrationeller Koordinaten, eine entscheidende Rolle in diesen Prozessen, da alle chemischen Reaktionen in ihrem Verlauf die Anordnung der Kerne im Molekül verändern. Beispielsweise wird der Energietransfer in den ersten Schritten der Photosynthese durch vibrationelle Bewegung herbeigeführt. Außerdem trägt die Kopplung von Vibrationen an elektronische Übergänge, wie sie durch das Frank-Condon Prinzip beschrieben wird, maßgeblich zu Spektren im sichtbaren Spektralbereich bei und ist daher für deren Interpretation und Auswertung unerlässlich. Ihre entscheidende Bedeutung erfordert eine profunde Beschreibung und Untersuchung vibrationeller Beiträge in zeitaufgelösten elektronischen Spektren.

Diese Arbeit beschäftigt sich mit solchen Beiträgen, die mittels heterodyn detektierter Transienter-Gitter-Spektroskopie von Hypericin gemessen werden. Da die Modulation der elektronischen Spektren durch Schwingungen in der Zeitdomäne aufgezeichnet wird ist es möglich, sowohl ihre Amplitude als auch ihre Phase in Abhängigkeit der Detektionswellenlänge darzustellen. Den entsprechenden Spektren werden theoretische Vorhersagen gegenübergestellt, deren Grundlage die sehr universelle nichtlineare optische „Response“ - Theorie darstellt, die eine valide und besonders aufschlussreiche Alternative zur häufigeren Behandlung im Wellenpaket-Formalismus darstellt. Die in dieser Arbeit dargelegte Methodik erklärt nicht nur die experimentell erhaltenen Spektren, sondern ist darüber hinaus auf eine große Bandbreite anderer Moleküle als Hypericin, auch in anderem als gelöstem Zustand, anwendbar. Beispielsweise wäre die Untersuchung vibrationell-elektronischer Kopplung im Energietransfer in Lichtsammelkomplexen eine logische Fortsetzung dieser Arbeit.

Abbreviations and Symbols

2D	... Two dimensional
2D-ES	... Two dimensional electronic spectroscopy
(Het-)TG	... (Heterodyne detected) transient grating spectroscopy
PP	... Pump probe spectroscopy = transient absorption spectroscopy
FWM	... Four wave mixing
VC	... Vibrational coherence
FC	... Franck-Condon
LO	... Local oscillator
NOPA	... Noncollinear optical parametric amplifier
CW	... Continuous wave
FWHM	... Full width at half maximum
FROG	... Frequency resolved optical gating
OD	... Optical density
DAS	... Decay associated spectrum
RR	... Resonant Raman
DFT	... Discrete Fourier transform
$FC_{m,n}$... Franck-Condon factor
AU	... Decadic Absorption units
ρ	... Density matrix
r	... Position
t	... time
E	... Electric field / Electric field amplitude of an electromagnetic wave
I	... Intensity
ε	... Energy
ω	... Frequency; radian frequency in formulas, ordinary frequency in experimental results
λ	... Wavelength
τ	... Period
k	... Wavevector
μ	... Dipole operator
μ_{nm}	... Transition dipole moment
$S^{(\alpha)}$... α^{th} order response function (if α is not specified, $\alpha = 3$)
$R_{\beta}^{(\alpha)}$... α^{th} order Liouville space pathway (if α is not specified, $\alpha = 3$)
J	... Auxiliary function
δ_{mn}	... Kronecker delta

δ	... Delta function
d	... Curve displacement
D	... Huang-Rhys factor
A	... Amplitude
φ	... Phase

Contents

1	Introduction	1
2	Theory	3
2.1	Theory of nonlinear optical spectroscopy - response theory	3
2.1.1	The density matrix	3
2.1.2	Equations of motion for the density matrix and their solutions.....	4
2.1.3	Response functions, pathways and their graphical representation	6
2.1.4	Pulsed excitation fields provide time ordering	9
2.1.5	Directionality of third order signals	9
2.1.6	Classification of pathways and their signals.....	10
2.1.7	Absorptive and dispersive signal contributions.....	11
2.2	Third order nonlinear experiments	13
2.2.1	2D electronic spectroscopy.....	13
2.2.2	Transient Grating spectroscopy	15
2.2.3	Pump Probe spectroscopy.....	15
2.2.4	Heterodyne detection – recovering absorptive and dispersive signal fields.....	16
2.3	Vibrational signatures in electronic spectroscopy	17
2.3.1	Vibrational progressions.....	17
2.3.2	The Franck-Condon principle, Franck-Condon factors.....	18
2.3.3	The displaced harmonic oscillator.....	19
3	Experimental	22
3.1	Pulse generation and compression.....	22
3.2	Pulse characterization.....	23
3.3	Experimental apparatus	24
3.3.1	2D-ES and Het-TG.....	24
3.3.2	Pump Probe	25
3.4	Experimental procedures	25
3.4.1	Sample preparation.....	25
3.4.2	Pump Probe spectroscopy.....	26
3.4.3	2D Electronic Spectroscopy and Heterodyned Transient Grating.....	26
3.4.4	Steady state experiments	27
3.5	Data Processing and Analysis	27
3.5.1	Pump Probe	27
3.5.2	Data processing of Het-TG and 2D-ES; phasing.....	28
3.5.3	Further analysis of 2D-ES	29
3.5.4	Analysis of vibrations in Heterodyned Transient Grating.....	29

3.5.5	Model for fitting of hypericin's absorption spectrum.....	31
4	Results	33
4.1	Steady state spectroscopy	33
4.2	Pump Probe spectroscopy.....	34
4.3	2D-ES	35
4.4	Het-TG.....	36
4.4.1	Vibrations in Het-TG spectra	37
5	Discussion	40
5.1	Advantages and experimental aspects of Het-TG in comparison to PP	40
5.2	Data analysis, retrieval of vibrational amplitude and phase	41
5.3	Analysis of vibrational coherence in Het-TG.....	41
5.3.1	Theoretical predictions for a displaced harmonic oscillator model within the impulsive limit	42
5.3.2	Non-impulsive excitation	46
5.3.3	Finite line-widths, vibrational coherence in absolute and dispersive TG signals.....	47
6	Conclusion.....	49
	Appendix	50
	Appendix A. Calculation of the first order polarization of a two level system	50
	Appendix B. Evaluation of time domain GA for the retrieval of oscillatory phase- and amplitude spectra.....	51
	Appendix C. Ground state vibrational coherence and the impulsive limit.....	54

1 Introduction

Time resolved spectroscopy in the visible and infrared regime is a routinely used tool for qualitative and quantitative chemical analysis. Consecutive recording of optical spectra, such as absorption -, fluorescence - or Raman scattering spectra, provides insights into the evolution of chemical reactions along their reaction coordinates and supplies the experimentalist with easy to interpret data. In such applications the timescales of interest are those of chemical reactions on a macroscopic scale as described by kinetic rate laws, ranging from days to ms in most conventional applications. The situation is fundamentally different when studying processes on a molecular level, *i.e.* when taking the step from the investigation of chemical rates to mechanistic studies of chemical and physical processes. This change of perspective is often referred to as the step from chemical kinetics to chemical dynamics. Research of the latter kind aims at “snapshots” *of* a process *in* the process. Such snapshots record, amongst others, the energetic distribution and the position of nuclei within a molecule and enable the study of isomerisation reactions [1,2], intra- and intermolecular proton- and electron transfer [3–5] and energy transport phenomena, which play a major role in photosynthesis [6–8].

The temporal resolution necessary for these studies is mostly given from the timescales of nuclear motion. These can be estimated from the well known vibrational modes typically observed in infrared absorption spectra. For example, a C=C - stretch vibration of 1600 cm^{-1} has a period of 21 fs ($1\text{ fs} = 10^{-15}\text{ s}$). Such extreme temporal resolutions require a precise timing of both, the event initiating the studied process and the probing of the ongoing process. In nonlinear optical spectroscopy ultrashort laser pulses of typical duration on the order of 10 fs are used to meet these criteria. These pulses not only provide the required temporal resolution but enable multidimensional nonlinear spectroscopic experiments that yield extremely rich information inaccessible to any other technique. Their development was inspired by multidimensional NMR spectroscopy, which, just as the techniques described in this thesis, employs carefully designed sequences of impulsive excitations to prepare the sample, *e.g.* a collective of dissolved molecules, in well defined states which’s temporal evolution can then be studied. The most intuitive and still most widely used ultrafast spectroscopic technique is *pump probe* or *transient absorption spectroscopy* (PP). In PP a pump pulse prepares the system in an excited state whose spectral absorption and emission is recorded by a probe pulse after varying waiting times. PP therefore extends linear absorption and emission spectra of transient species onto a femtosecond time axis. [2,9,10] An even richer level of information can be achieved by exploiting the full range of nonlinear optical spectroscopic techniques (see VAUTHEY [11] for an overview). In this thesis we will employ two dimensional electronic spectroscopy (2D-ES) and heterodyned transient grating spectroscopy (Het-TG), which are variants of four wave mixing (FWM) [12–14] that will be explained below. The examined spectral regime is situated in the visible, hence electronic spectra are

Introduction

recorded, *i.e.* spectra associated with changes in electronic quantum numbers. Although light of such wavelengths is not in resonance with molecular vibrations, electronic spectra are strongly influenced by nuclear degrees of freedom. [15] The interplay between nuclear and electronic degrees of freedom in electronic transitions was investigated by FRANCK and CONDON [16,17] who explained how quasi-instantaneous electronic transitions can initiate molecular vibrations. In a quantum mechanical description, this is stated as the creation of vibrational coherences (VC), *i.e.* coherent superpositions of quantum mechanical vibrational states. VC on the electronic excited state can play an important role in photoreactivity and energy transport. For example, it was demonstrated recently that ultrafast energy transport in natural light harvesting complexes can be explained by the interplay of electronic and vibrational degrees of freedom while purely electronic coupling mechanisms failed to do so. [7] In addition to its participation in the studied processes, excited state VC can also serve as a probe for molecular structure of the initial excited state and possible product states that are populated from it [18].

The remarkable role of vibrations in molecular processes motivates the study of vibrational signatures in ultrafast electronic spectroscopy presented in this thesis. We investigate VC in heterodyned transient grating spectra of hypericin. Hypericin [19] is a natural photosensitizer that can be extracted from *Hypericum perforatum* (“St. Johns wort”) and other members of the *Hypericum* genus. As a photosensitizer it chemically reacts with its surrounding upon illumination. Hypericin acidifies its chemical environment, produces singlet oxygen and is subject of ongoing research due to its antiviral effects. [20–22] On the timescales of our experiments (50 fs to 40 ps) and in the spectroscopic techniques we employed, however, hypericin did not show clear signatures of photo-initiated reactions. We did, however, observe VC of multiple modes. We therefore employed hypericin as a model molecule to investigate the signatures of VC in ultrafast electronic Het-TG spectroscopy.

We investigate the amplitude and phase of oscillatory signals arising from VC as a function of optical detection frequency for multiple vibrational modes of frequencies up to 1300 cm^{-1} . The results are interpreted within the theoretical frame work of response theory and the Franck-Condon (FC) principle. Response theory for optical spectroscopy provides a unified description of all kinds of linear and nonlinear optical spectroscopy. [12] The key concepts of the theory will be reviewed. By applying the FC principle to a displaced harmonic oscillator model and combining the results with response theory we find analytic explanations for experimental observations. A discussion of experimental constraints and their effects on the formation and probing of VC is provided.

In short, we use a nonlinear response theory based analytical approach to explain signatures of vibrations in time resolved electronic spectra as measured by heterodyned transient grating spectroscopy. While the approach is equivalent to the more widespread wavepacket formalism, the versatility of nonlinear response theory makes it applicable to a much wider range of nonlinear spectroscopic techniques and samples than covered by this thesis.

2 Theory

This chapter will provide the theoretical background necessary for the discussion provided in chapter 5 of vibrational signals in ultrafast spectra presented in chapter 4. Furthermore, the principles of nonlinear spectroscopic techniques used for this thesis will be explained.

Sections 2.1.1 and 2.1.2 set the stage for section 2.1.3, in which we introduce response functions and their graphical representations, double sided Feynman diagrams, which will prove to be a valuable tool for the discussion of third order signals in chapter 5. Sections 2.1.4 to 2.1.7 deal with concepts relevant for chapter 5 and for the experiments introduced in section 2.2. In section 2.3 the role of vibrations in electronic spectra is discussed and the Franck-Condon principle is introduced, which we apply to the model of a displaced harmonic oscillator.

2.1 Theory of nonlinear optical spectroscopy - response theory

To understand the techniques of femtosecond nonlinear spectroscopy discussed in the following and some of its peculiarities, such as the emission of signal fields in directions different to incident beams, we must discuss some theory of nonlinear spectroscopy. We will thereby stay in the framework of nonlinear response theory which, due to its versatility and completeness, is to date the workhorse for both, experimentalists and theoreticians in the field of nonlinear optical spectroscopy. [12] Our derivations in the first three sections will mostly follow REZUS [23]. We also want to point to the TOKMAKOFF – lecture notes [24] on time dependent quantum mechanics and spectroscopy as a reference for the following discussion.

Within response theory optical spectroscopic experiments are interpreted in the following manner: One or multiple interactions with an electromagnetic field induce a polarization $P(r,t)$ in the molecular system under study. This polarization, if not stationary, acts as a source of a radiation field, which is referred to as “signal field”, according to Maxwell equations. Depending on the experiment the signal field may be emitted in a unique direction or overlap with incident fields before its intensity is measured. The molecular system influences the experiments only through the polarization. Response theory connects the induced polarization quantum mechanically to the system’s properties and the electric fields used to probe them. In other words, response theory describes molecular dynamics as probed by (ultrafast) optical spectroscopy.

2.1.1 The density matrix

$P(r,t)$ is usually calculated semi-classically. The electromagnetic fields are treated classically while the system is described by time dependent quantum mechanics. From the system’s wave function, within the dipole approximation, $P(r,t)$ can be calculated as the expectation value of the dipole operator μ

$$\mu = \sum_j q_j (\mathbf{r} - \mathbf{r}_j) \quad (2.1)$$

$$P = \langle \Psi | \mu | \Psi \rangle = \text{Tr}(\mu \rho). \quad (2.2)$$

Theory

Herein, q_j represents the charge and r_j the position, expressed in molecular coordinates, of the particle j of the system. Tr stands for the tracing operation. In Eq.(2.2) and throughout this work we use bracket notation for quantum mechanical representations [25,26]. The molecular system can be described by its wavefunction $|\Psi\rangle$ or by a density matrix [24]

$$\rho := |\Psi\rangle\langle\Psi|. \quad (2.3)$$

The matrix elements of ρ are given by

$$\rho_{nm} = \langle n | \rho | m \rangle, \quad (2.4)$$

where $|n\rangle$ and $|m\rangle$ are basis vectors. Most commonly, the wavefunction $|\Psi\rangle$ and its complex conjugate $\langle\Psi|$ are given in an orthonormal eigenfunction basis, $|\Psi\rangle = \sum_n c_n |n\rangle$. This makes the

density matrix elements take the form $\rho_{nm} = c_n c_m^*$ and easy to interpret. In accordance to response theory we will in the following make use of the density matrix, mostly because it allows us to interpret nonlinear spectra using an intuitive diagrammatic approach, *i.e.* double sided Feynman diagrams, and because it allows for the representation of mixed states, *i.e.* statistical states of an ensemble of molecules, which is essential, amongst others, for the description of solvated molecules interacting with the solvent (“*bath*”). When employing the density matrix in quantum mechanical descriptions one works within the so called *Liouville space* [12]. The time dependence of the system and therefore its time-dependent polarization is described through the dynamics of the density matrix elements. Based on their temporal behaviour it is useful to distinguish diagonal elements ρ_{nn} (“*populations*”) and off-diagonal elements ρ_{nm} (“*coherences*”). The former represent eigenstates $|n\rangle$ and evolve slowly, while the latter represent superpositions of eigenstates $|n\rangle$ and $|m\rangle$ which oscillate according to the energy difference $\omega_{nm}\hbar$ between the eigenstates and show up in spectroscopic experiments at their according frequency ω_{nm} .

2.1.2 Equations of motion for the density matrix and their solutions

Where the temporal evolution of $|\Psi\rangle$ is described by the Schrödinger equation, the time dependency of ρ is given by the *Von Neumann* - equation Eq.(2.5), which naturally arises from the Schrödinger equation and the definition Eq.(2.3) of ρ [24]

$$\frac{\partial \rho}{\partial t} = \frac{-i}{\hbar} [\hat{H}, \rho] = \frac{-i}{\hbar} (\hat{H} \rho - \rho \hat{H}). \quad (2.5)$$

Herein, square brackets denote a commutator and \hat{H} is the full Hamiltonian of the system. In the presence of an electromagnetic field perturbing the pure system Hamiltonian,

$$\hat{H}_0 = \sum_n \varepsilon_n |n\rangle\langle n|, \quad (2.6)$$

Theory

where ε_n are the system's eigenvalues of energy, the Hamiltonian can be written as (within the dipole approximation)

$$\hat{H} = \hat{H}_0 + \hat{V}(t) = \hat{H}_0 - \mu E(t) \quad (2.7)$$

and the *Von Neumann* - equation for a given density matrix element reads [23]

$$\frac{\partial \rho_{nm}}{\partial t} = -i\omega_{nm}\rho_{nm} + \frac{i}{\hbar} E(t)[\mu, \rho]_{nm}. \quad (2.8)$$

Note that Eq.(2.8) and all further discussions neglect dephasing in the oscillatory part $-i\omega_{nm}\rho_{nm} = -i\rho_{nm}(\varepsilon_n - \varepsilon_m)/\hbar$. Therefore all equations presented in the following do not include lineshapes and all spectra would be stick spectra. Lineshapes can be included by adding a term \hat{H}_{bath} in Eq.(2.7) which accounts for interactions of the system with its surrounding, most commonly the solvent [27]. A very basic discussion on lineshapes will be given in the context of absorptive - and dispersive signals in chapter 2.1.7.

At this point it is necessary to expand $\rho = \rho_{eq} + \rho^{(1)} + \rho^{(2)} + \rho^{(3)} + \dots$. We will use the elements of this expansion to discuss signals produced by the corresponding polarization $P = P_{eq} + P^{(1)} + P^{(2)} + P^{(3)} + \dots$. We will show that the expansion elements correspond to the number of interactions with fields E and that the third order elements describe signals measured in pump probe, transient grating, 2D electronic spectroscopy and other four wave mixing experiments.

Applying Eq. (2.8) to the expansion yields a set of coupled differential equations

$$\frac{\partial \rho_{nm}^{(1)}}{\partial t} = -i\omega_{nm}\rho_{nm}^{(1)} + \frac{i}{\hbar} E(t)[\mu, \rho_{eq}]_{nm} \quad (2.9)$$

$$\frac{\partial \hat{\rho}_{nm}^{(2)}}{\partial t} = -i\omega_{nm}\rho_{nm}^{(2)} + \frac{i}{\hbar} E(t)[\mu, \rho^{(1)}]_{nm} \quad (2.10)$$

$$\frac{\partial \hat{\rho}_{nm}^{(3)}}{\partial t} = -i\omega_{nm}\rho_{nm}^{(3)} + \frac{i}{\hbar} E(t)[\mu, \rho^{(2)}]_{nm} \quad (2.11)$$

$$\frac{\partial \hat{\rho}_{nm}^{(\alpha)}}{\partial t} = -i\omega_{nm}\rho_{nm}^{(\alpha)} + \frac{i}{\hbar} E(t)[\mu, \rho^{(\alpha-1)}]_{nm}$$

Integration over the full history of the system, i.e. from $-\infty$, yields

$$\rho_{nm}^{(1)}(t) = \frac{i}{\hbar} \int_{-\infty}^t d\tau_0 \exp(-i\omega_{nm}(t - \tau_0)) E(\tau_0) [\mu, \rho_{eq}(\tau_0)]_{nm} \quad (2.12)$$

$$\rho_{nm}^{(2)}(t) = \frac{i}{\hbar} \int_{-\infty}^t d\tau_1 \exp(-i\omega_{nm}(t - \tau_1)) E(\tau_1) [\mu, \rho^{(1)}(\tau_1)]_{nm} \quad (2.13)$$

$$\rho_{nm}^{(3)}(t) = \frac{i}{\hbar} \int_{-\infty}^t d\tau_2 \exp(-i\omega_{nm}(t - \tau_2)) E(\tau_2) [\mu, \rho^{(2)}(\tau_2)]_{nm} \quad (2.14)$$

Theory

$$\rho_{nm}^{(\alpha)}(t) = \frac{i}{\hbar} \int_{-\infty}^t d\tau_{\alpha-1} \exp(-i\omega_{nm}(t-\tau_{\alpha-1})) E(\tau_{\alpha-1}) [\mu, \rho^{(\alpha-1)}(\tau_{\alpha-1})]_{nm} . \quad (2.15)$$

Herein τ_j is an integration variable that indicates the moment at which the j^{th} dipole interaction of the system with the electric field occurs. Note that $\tau_0 \leq \tau_1 \leq \dots \leq \tau_{\alpha-1}$. Because ρ_{eq} is assumed stationary the moment of first interaction τ_0 is arbitrary and we therefore only care for the intervals $t_\alpha = \tau_\alpha - \tau_{\alpha-1}$.

2.1.3 Response functions, pathways and their graphical representation

We now turn to a discussion of the structure of Eq.(2.15). This will not only prove insightful but allow us to introduce the response function and “(Liouville space) pathways”, leading to a graphical representation called “double sided Feynman diagrams.” We will then demonstrate how transition dipole moments enter the equations and scale the signals, which is a key aspect for the discussion of VC in chapter 5.

Firstly, Eq.(2.12) - (2.15) are nested equations since $\rho^{(\alpha)}$ depends on $\rho^{(\alpha-1)}$. This structure represents a natural evolution of $\rho^{(\alpha)}$ arising from $\rho^{(\alpha-1)}$ upon dipole interaction with E , so that for every $\rho_{nm}^{(\alpha)}$ one can follow the paths through the lower order density matrices down to ρ_{eq} that lead to the population of $\rho_{nm}^{(\alpha)}$. The number of trajectories leading to $\rho_{nm}^{(\alpha)}$ depends on the number of dipole accessible states of the system and on α .

Secondly, $\rho^{(\alpha)}$ and hence $P^{(\alpha)} = \text{Tr}(\mu \rho^{(\alpha)})$ scale with E^α . The power α in the external field E determines the order of the signal and the order of spectroscopy it facilitates.

Thirdly, the density matrix $\rho^{(\alpha)}$ constituted of the elements described by Eq.(2.15) can be expressed as a sum of 2^α terms based on the commutators in Eq.(2.12) - (2.15). These terms differ from each other in their sign and the sequence of sides of the density matrix on which μ is multiplied. The latter aspect is usually stated as the dipole operator acting on the $\langle \text{bra} |$ - (right) or $| \text{ket} \rangle$ side (left) of the density matrix. These 2^α permutations correspond to the same number of (Liouville space) pathways $R_\beta^{(\alpha)}$.

In Appendix A we demonstrate for a two level system the evaluation of $P^{(1)}(t) = \text{Tr}(\mu \rho^{(1)}(t))$ to illustrate the above mentioned findings and to demonstrate how the dipole operator in Eq.(2.9) - (2.15) is replaced by transition dipole moments μ_{nm} in the pathways $R_\beta^{(\alpha)}$.

Generally speaking, the α^{th} order (non)linear response function $S^{(\alpha)}$ and the pathways $R_\beta^{(\alpha)}$ are defined in a way that allows expressing $P^{(\alpha)}$ as (compare Appendix A or [23])

$$P^{(\alpha)}(t) = \int_0^\infty dt_\alpha \dots \int_0^\infty dt_1 S^{(\alpha)}(t_1, t_2, t_3) E(t-t_\alpha) E(t-t_\alpha-t_{\alpha-1}) \dots E(t-t_\alpha-\dots-t_1) \quad (2.16)$$

Theory

$$S^{(\alpha)}(t_1, t_2, \dots, t_\alpha) = \sum_{\beta=1}^{2^\alpha} R_\beta^{(\alpha)}(t_1, t_2, \dots, t_\alpha) = \sum_{\beta=1}^{2^{\alpha-1}} R_\beta^{(\alpha)}(t_1, t_2, \dots, t_\alpha) + c.c. \quad (2.17)$$

In Eq.(2.17) we made use of the fact that for any pathway there is a pathway representing the complex conjugate of it.

To first order, $R_\beta^{(1)}$ are given in Appendix A. To third order, $R_\beta^{(3)}$ are given by Eq. - (adopted from REZUS [23], Eq.(2.34) - (2.37))

$$R_1^{(3)}(t_1, t_2, t_3) = \sum_{abcd} \rho_{eq,aa} \mu_{db} \mu_{cd} \mu_{ac} \mu_{ba} J_{bd}(t_3) J_{bc}(t_2) J_{ba}(t_1) \quad (2.18)$$

$$R_2^{(3)}(t_1, t_2, t_3) = \sum_{abcd} \rho_{eq,aa} \mu_{dc} \mu_{bd} \mu_{ca} \mu_{ab} J_{cd}(t_3) J_{cb}(t_2) J_{ab}(t_1) \quad (2.19)$$

$$R_3^{(3)}(t_1, t_2, t_3) = \sum_{abcd} \rho_{eq,aa} \mu_{cd} \mu_{da} \mu_{bc} \mu_{ab} J_{dc}(t_3) J_{ac}(t_2) J_{ab}(t_1) \quad (2.20)$$

$$R_4^{(3)}(t_1, t_2, t_3) = \sum_{abcd} \rho_{eq,aa} \mu_{ad} \mu_{dc} \mu_{cb} \mu_{ba} J_{da}(t_3) J_{ca}(t_2) J_{ba}(t_1) \quad (2.21)$$

Herein, we introduced the transition dipole moment

$$\langle n | \mu | m \rangle = \mu_{nm} \quad (2.22)$$

and the auxiliary function $J_{nm}(t)$, which for the Hamiltonian described by Eq.(2.7) reads

$$J_{nm}(t) = \exp(-it(\varepsilon_n - \varepsilon_m)/\hbar) = \exp(-it\omega_{nm}). \quad (2.23)$$

The auxiliary function represents the evolution of ρ^α during t_α . The transition dipole moment μ_{nm} gives the probability of a dipole induced transition from $|m\rangle\langle a|$ to $|n\rangle\langle a|$ or from $|a\rangle\langle n|$ to $|a\rangle\langle m|$.

The differences between the various pathways $R_\beta^{(3)}$ will be discussed in section 2.1.6. The sums in Eq.(2.18) - (2.21) represent all possible trajectories $\rho_{eq,aa} \rightarrow \rho_{n_1 m_1}^{(1)} \rightarrow \rho_{n_2 m_2}^{(2)} \rightarrow \rho_{n_3 m_3}^{(3)}$ through the different order density matrices. The sum of all possible trajectories gives $S^{(3)}(t_1, t_2, t_3)$.

A popular and highly useful representation of these trajectories are *double sided Feynman diagrams* [28]. An example for a double sided Feynman diagram is presented in Figure 1a. The diagram is to be read from bottom to top and illustrates the temporal evolution of the density matrix through its increasing orders. Solid arrows represent the dipole operator acting on the density matrix, *i.e.* the interaction of the system with light preparing the density matrix $\rho^{(\alpha)}$ from $\rho^{(\alpha-1)}$. Between two interactions $\rho^{(\alpha)}$ evolves for a time t_α . After three interactions the density matrix $\rho^{(3)}$, then reading $|e\rangle\langle g|$ in Figure 1a, gives rise to a third order polarization $P^{(3)}(t_3)$ oscillating at the frequency ω_{eg} and a corresponding signal E_s . This signal field is represented by a dashed arrow and the density matrix after the emission of the signal is given at the top of the diagram.

Theory

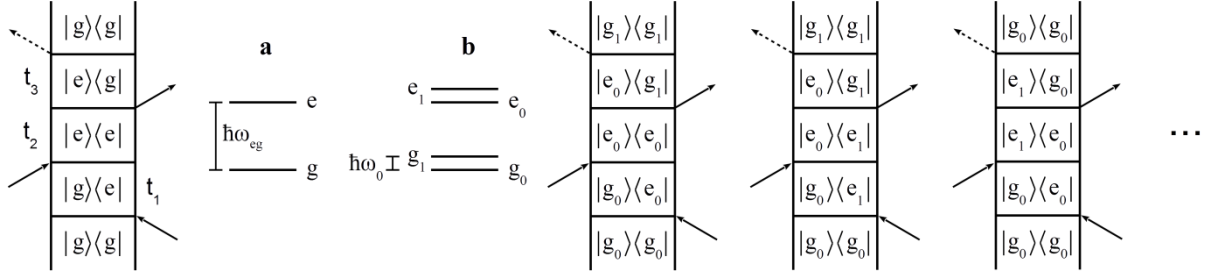


Figure 1. **a**, left: example for a double sided Feynman diagram representing a stimulated emission pathway in a two level system $|g\rangle, |e\rangle$, illustrated by its energy level diagram (right). **b**, further diagrams for the same pathway in a system with two electronic levels each with one additional vibrational level.

Double sided Feynman diagrams not only simplify the interpretation of nonlinear spectroscopic signals, but can be evaluated in an exact analytic manner to give a summand of the underlying pathway $R_\beta^{(3)}(t_1, t_2, t_3)$. If all possible diagrams are evaluated one obtains the full response function $S^{(3)}(t_1, t_2, t_3)$. The rules of evaluation are given in [12]. The basic rules relevant for writing and reading such diagrams are as follows: The arrows' directions indicate the sign of the signals wavevector with respect to the wavevector of the interacting field. This determines the direction in which the signal is emitted, as will be discussed in section 2.1.5. Inward (outward) pointing arrows indicate an absorption (emission) event. By convention, the signal field is always emitted from the left (ket) side. Due to the definition of the commutator, interactions with a bra (right side) carry a negative sign, such with a ket (left side) a positive sign. Hence, the overall sign of a diagram is given by $(-1)^n$, where n is the number of right- (bra-) side interactions. This sign corresponds to the phase of the signal field with respect to the field of the third interaction. The density matrix after the emission of the signal must be in a population state since coherences vanish too rapidly.

In general, a single pathway has many diagrams because the density matrix in each period can take many different forms, depending on the number of dipole accessible states of the system. This is illustrated in Figure 1b in which the system is composed of four vibronic eigenstates. In practice, the number of dipole accessible states is not only limited by the molecular system but by finite spectra $E(\omega)$ driving the transitions.

As an example of $R_\beta^{(3)}$ the pathway $R_1^{(3)}(t_1, t_2, t_3)$ for the two level system in Figure 1a is given in Eq.(2.24). Since the system is constituted of only two levels and only the ground state is assumed to be populated in equilibrium, only a single diagram contributes to the pathway $R_1^{(3)}(t_1, t_2, t_3)$.

$$R_1^{(3)}(t_1, t_2, t_3) = |g\rangle\langle g| \mu_{eg} \mu_{ge} \mu_{ge} \mu_{eg} \exp(-i\omega_{eg} t_1) I_{ee}(t_2) \exp(-i\omega_{eg} t_3). \quad (2.24)$$

Within the assumption made in Eq.(2.7), $J_{ee}(t_2) = 1$. More generally, $J_{nm}(t_2)$ denotes molecular dynamics in t_2 that is to be studied. While the evolution in t_1 and t_3 is oscillatory with $\omega_{eg} = -\omega_{ge}$ corresponding to optical frequencies, $J_{nm}(t_2)$ is non-oscillatory ($\omega_{ee} = 0$). The situation is slightly different in Figure 1b: The additional vibrational levels allow for second order density matrices

Theory

$\rho^{(2)}(t_2)$ that evolve as $\exp(-i\omega_0 t_2)$ in t_2 , i.e. diagrams that yield signals that oscillate at vibrational frequencies $|\omega_{e_1 e_0}| = |\omega_{e_0 e_1}| = \omega_0$ in t_2 . These signals will be discussed in great detail in this thesis. The finding that the system is in a rapidly oscillating coherence state during the intervals t_1 and t_3 but slowly evolves during t_2 (population) is true for all pathways relevant to the experiments described below. Therefore t_1 and t_3 are referred to as coherence times, t_2 as population time (even if the system is in a vibrational coherence during t_2).

2.1.4 Pulsed excitation fields provide time ordering

Before being able to connect the double sided Feynman diagrams to spectra observed in third order nonlinear spectroscopic techniques described below we need to briefly discuss how t_1 , t_2 and t_3 can be controlled in experiments. So far we have made no assumptions about the electric field driving the described processes. Therefore we could not specify the moments in which the system and the field interact and it was necessary to integrate over all possible intervals t_1 , t_2 and t_3 in Eq.(2.16).

We will now assume, in accordance with the experiments described below, that the electric field is composed of three short pulses whose temporal peak power and phases are controlled individually. If the pulses do not overlap temporally the order in which they interact with the system is fixed. If we additionally ensure that each pulse interacts with the system only once, which can be done by exploiting the phase matching condition described below, we can essentially control t_1 and t_2 , which are then defined as the temporal peaks of the second and third pulse relative to the first one. The experiment therefore limits the time ranges that have to be integrated in Eq.(2.16) and nicely reflects the double sided Feynman diagram up to the third interaction (after t_2). The last time interval t_3 is not controlled in the sense of t_1 or t_2 but instead measured indirectly by recording the signal $E(t_1, t_2, \omega_3)$ using a spectrometer dispersing the signal field onto a camera. ω_a and t_a form Fourier transform pairs, hence the relation between $E(t_1, t_2, t_3)$ and $E(\omega_1, t_2, \omega_3)$, the most common representation of third order nonlinear signals, as well as $S^{(3)}(t_1, t_2, t_3)$ and $S(\omega_1, \omega_2, \omega_3)$, is established. The representation in ω_1, t_2, ω_3 is chosen due to the oscillatory evolution in t_1 and t_3 and the slow evolution in t_2 discussed for Eq.(2.24).

2.1.5 Directionality of third order signals

We now turn to the directionality of the signal fields arising from the directionality of the fields interacting with a spatially extended sample. It turns out that different (third order) pathways Eq.(2.18) - (2.21) emit signals in different directions. This is exploited experimentally in four wave mixing (FWM) experiments, such as Het-TG and 2D-ES introduced in section 2.2, to detect third order signals selectively and background free [13]. We limit ourselves to giving a simple rule for the signals direction, *the phase matching condition*, and to an explanation of how to apply this rule to double sided Feynman diagrams. A more rigorous treatment is provided by HAMM and ZANNI. [29]

Theory

To describe the directional properties of the signal field and the excitation fields (excitation pulses) we introduce their wavevectors k_{sig}, k_1, k_2 and k_3 . For isotropic samples of low concentration the individual molecules do not affect each other [12] and the directionality of the signal field only depends on the excitation pulses' wavevectors via the *phase matching condition* [29,30]

$$k_{sig} + k_1 + k_2 + k_3 = 0. \quad (2.25)$$

The signs of the wave vectors in the phase matching condition depend on the pathway and can be directly read from the double sided Feynman diagrams, more precisely from the pointing of the arrows ('-' for left pointing, '+' for right pointing arrows). For the pathway shown in Figure 1 this results in

$$k_{sig} = -k_1 + k_2 + k_3. \quad (2.26)$$

If the pointing of the wavevectors of the three excitation pulses differ from each other, as is the case in FWM, different pathways emit fields in different directions. Placing the detector in a phase matched direction not only greatly reduces the number of pathways $R^{(3)}$ that have to be considered but additionally gets rid of any contributions from lower order polarizations (if the phase matched direction does not coincide with k_1, k_2 or k_3) or from the excitation pulses themselves. The signal field along k_{sig} is then detected free of background contributions such as fluorescent light or excitation pulses.

Intuitively, the phase matching condition can be understood as a consequence of the pulses imprinting their spatial phases, *i.e.* their wave vectors, onto the volume under study, creating a “transient grating”. [13] This makes the source of the signal field of a pathway a lattice (or grating, hence Transient grating spectroscopy, section 2.2.2), from which the directionality of the signal results. Simply put, the phase of light emitted from the individual molecules is not randomly distributed in the sample volume, but coherent with the excitation pulses and therefore coherent throughout the excitation volume.

2.1.6 Classification of pathways and their signals

We discussed in the previous chapter how one can control and pick pathways by time ordering the pulses and choosing non-collinear excitation pulses. We will now explain how the pathways differ from each other and which properties of the system they probe.

The first possible classification can be made into rephasing and non-rephasing pathways. This term describes the relation between the coherences during the intervals t_1 and t_3 . In t_3 the system can either be in a state that is the complex conjugate to the state during the t_1 -interval, e.g. $|g\rangle\langle e|$ and $|e\rangle\langle g|$, or in a state that resembles the state during t_1 , e.g. $|e\rangle\langle g|$ and $|e\rangle\langle g|$. The first case shown in Figure 2, R_1 , is called “rephasing”, the latter “non-rephasing” (Figure 2, R_2). Rephasing pathways produce so-called photon echo signals, representing the optical analogue to spin echoes known from 2D-NMR spectroscopy [31]. A detailed description of photon echoes utilizing Bloch vectors is given in chapter 2.6 of [29]. In essence, photon echoes are produced when the t_1 -evolution of an inhomogeneous

Theory

ensemble is reversed in t_3 , leading to a synchronous return of the ensemble to the phase of $t_1 = 0$ at $t_3 = t_1$. This rephasing process gives rise to a macroscopic polarization and consequently the emission of the echo signal at $t_3 = t_1$. Non-Rephasing pathways do not invert the t_1 evolution and the signals therefore decay exponentially with t_3 and are, for moderate values of population time t_2 , in general weaker than rephasing signals. Note that for $t_1 = 0$ rephasing and corresponding non-rephasing pathways are identical as no evolution in t_1 is possible. This will prove important for pump probe and transient grating spectroscopy.

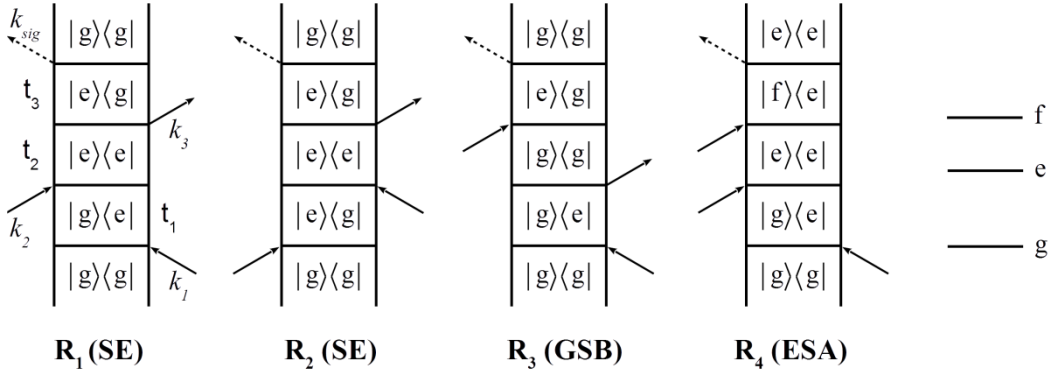


Figure 2. Examples of third order pathways represented by their double sided Feynman diagrams.

All pathways contributing to third order nonlinear signals emitted in the phase matched directions $k_{sig}^I = -k_1 + k_2 + k_3$ and $k_{sig}^{II} = k_1 - k_2 + k_3$, which are the directions in which signals are recorded in all third order spectroscopic experiments discussed below, can additionally be classified as *stimulated emission* - (SE), *ground state bleach*- (GSB) or *excited state absorption* (ESA) pathways. This categorisation allows a straight forward physical interpretation of the signals. In SE pathways the signal is generated via stimulated emission of a photon from an electronically excited state population $|e\rangle\langle e|$ during t_2 (R_1 and R_2 in Figure 2). If a dipole allowed transition to a higher lying state is possible, the excited state population $|e\rangle\langle e|$ can also give rise to ESA (R_4 in Figure 2). GSB signals are, especially in pump probe, commonly interpreted as a lack of absorption due to partial depopulation of the ground state by a preceding pulse. This interpretation, however, is problematic in four wave mixing experiments where the signals are measured directly as positive intensity in a phase matched direction, instead of a lack of intensity as in PP (compare section 2.2.3). The sign of the signals corresponding to the different pathways follows the rule described in section 2.1.3, given by $(-1)^n$, where n is the number of right- (bra-) side interactions. SE and GSB signals are positive while ESA signals are negative.

2.1.7 Absorptive and dispersive signal contributions

So far we assumed the evolution of the system during t_1 and t_3 to be purely oscillatory. Such evolution would yield stick spectra, the peaks in ω_1 and ω_3 would have no linewidth. Lineshapes as well as their

Theory

temporal evolution are, however, of outmost interest in the study of so called spectral diffusion [29], which gives insights into the interaction of a system with its surrounding [32]. Lineshapes are therefore extensively studied in 2D-ES [33] as well as 2D-Infrared spectroscopy [34]. In this chapter we will outline the origin of the signals' finite spectral width and thereby introduce absorptive and dispersive signals. A detailed discussion of the topic can be found in [29].

Finite line widths arise from a decay of the oscillating macroscopic polarization in the time domain. The origins of this decay are usually divided into inhomogeneous effects from a static distribution of oscillators of different frequencies and homogeneous effects arising from fast fluctuations in the (chemical) environment of a molecule and spontaneous relaxation, which will be similar for all molecules in the ensemble. [29] We will limit the discussion to homogeneous effects which can be described by exponential decays. An exponentially decaying oscillation of the form

$$E(t) = \theta(t) \times \cos(\omega_0 \times t) \times \exp(-t / \gamma) \quad (2.27)$$

is plotted in the time domain in Figure 3. Herein, $\theta(t)$ denotes the Heaviside step function, ensuring the causality of the signal “produced” by an interaction with an electromagnetic field at $t = 0$. The Fourier transform of this signal is given by the convolution, denoted by the $*$ - operator, of the Fourier transforms of the Heaviside step function, the cosine function and the exponential decay.

$$E(\omega) = \left[\frac{1}{2} \left(\delta(\omega) - \frac{2i}{\omega} \right) \right] * [\delta(\omega - \omega_0)] * \left[\frac{2 / \gamma}{1 / \gamma^2 + \omega^2} \right] \quad (2.28)$$

Herein, δ denotes the Dirac Delta. Square brackets indicate the Fourier transforms of the terms of Eq.(2.27).

It becomes clear and can be seen from Figure 3 that, in the frequency domain, this signal holds not only a finite distribution of cosine contributions, but also sine contributions. The jump of the imaginary part from positive to negative values at the central frequency ω_0 can be assigned to the Fourier transform of the Heaviside step function, *i.e.* the causality of the signal. Note that the phase of an oscillation is defined relative to the phase of the inducing field (first pulse for t_1 , second pulse for t_2 , third pulse for t_3). Cosine is in phase with the inducing field, sine out of phase (see. Eq.5.59 in [12]).

More commonly cosine and sine are described as real and imaginary parts in an Euler representation. The real part is called *absorptive* because it is linked to the transition from one state to the other in a molecular system and its corresponding transition frequency ω_0 . It is particularly useful for investigating population dynamics as its amplitude is proportional to the populations of the involved states. The imaginary part is referred to as *dispersive*. It is a measure for dephasing processes, e.g. the interaction of an oscillating molecule with its environment.

Theory

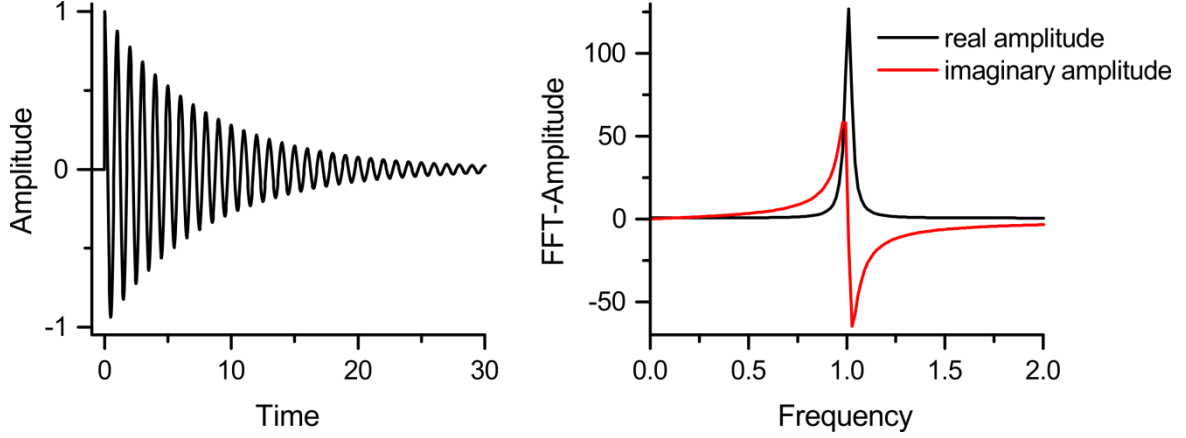


Figure 3. Origin of absorptive and dispersive signal contributions. Left: exponentially decaying oscillation in the time domain. Right: same signal in the frequency domain as obtained from Fast Fourier Transform. In the frequency domain the signal holds real (absorptive) and imaginary (dispersive) contributions.

An important practical aspect of these two signals is their linewidth. As can be seen from Figure 3 the absorptive peak is much narrower than the dispersive one. This makes it easier to distinguish spectral features that are in close proximity to each other in the absorptive parts of spectra.

Because of the different information content of absorptive and dispersive signal contributions and the superior resolving power of absorptive signals it is desirable to measure them separately. This is possible in a straight forward manner if the electric field of the signal is measured directly. Photo detectors can, however, only measure the field's intensity. We will discuss this aspect and the solution to this problem in section 2.2.4.

2.2 Third order nonlinear experiments

Three popular third order nonlinear spectroscopic experiments will be described in the context of third order nonlinear response theory: Two dimensional electronic spectroscopy [35], pump probe – and transient grating spectroscopy. Their experimental implementations, differences and other practical aspects will be discussed later.

2.2.1 2D electronic spectroscopy

We will start the discussion with two dimensional electronic spectroscopy (2D-ES) because firstly the other two techniques can be seen as a special case of 2D-ES, making it the most general of third order spectroscopic techniques. Secondly, the discussion of 2D-ES will illustrate how double sided Feynman diagrams can be used to interpret optical spectra.

The basic concept of 2D-ES is illustrated in Figure 4. Figure 4 **a** shows the boxcar geometry typical for four wave mixing (FWM) experiments such as 2D-ES. In 2D-ES the time intervals t_1 and t_2 defined by the delay of two ultra short pulses relative to a first one are scanned individually and the third order signal is measured spectrally resolved in the phase matched direction $k_{sig} = -k_1 + k_2 + k_3$.

Note that, in this case, k_1 , k_2 , k_3 refers to pulses in the experiment (compare Figure 4) and not

Theory

necessarily to time ordering. For rephasing pathways the time ordering illustrated in Figure 4 holds. When non-rephasing signals are to be measured, t_1 is chosen negative and k_2 precedes k_1 .

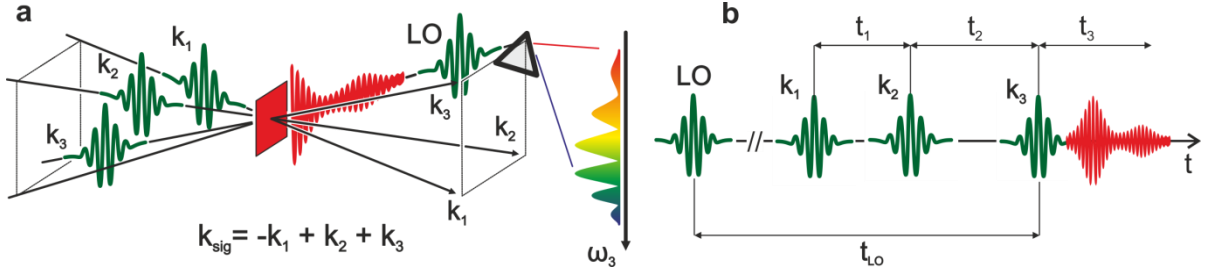


Figure 4. **a:** Illustration of two dimensional electronic spectroscopy and heterodyne transient grating experiments. Three pulses, k_1 , k_2 and k_3 (green lines), interact with the sample (red square section) which then emits a signal field (red line) in the phase matched direction k_{sig} . The signal field is mixed with a local oscillator pulse (LO) in a heterodyne detection scheme (compare section 2.2.4). **b:** Time ordering of the pulses in 2D-ES and Het-TG. For Het-TG $t_1 = 0$. Adapted from [36] with permission of the authors.

After Fourier transformation to $E_{sig}(\omega_1, t_2, \omega_3)$ the spectra are usually shown in a two dimensional contour plot with axis ω_1 and ω_3 for a single value of t_2 . A schematic 2D-ES map is shown in Figure 5. The simplest way to interpret these maps is in terms of correlations between excitation frequency ω_1 and emission frequency ω_3 . Diagonal peaks ($\omega_1 = \omega_3$) appear if the molecular system emits a field of the same frequency as it absorbed. Off diagonal elements indicate redistribution of energy in the system during t_2 as the excitation frequency does not match the emission frequency. Studying the evolution of 2D-ES maps with t_2 therefore makes it possible to follow the energy distribution in the molecular system with time. This makes 2D-ES an extremely powerful method for investigating a wide range of transfer processes, especially light harvesting in photosynthetic systems [6], and photoinduced chemical reactions [1].

A more profound interpretation of electronic 2D spectra utilizes double sided Feynman diagrams to link the evolution of the system to the position of signals in the ω_1 , ω_3 - maps. The connection between the system's states during t_1 , t_2 and t_3 and electronic 2D spectra is illustrated in

Figure 5. Circles indicate positions at which one expects signals of the four level system described in Figure 1b. The position in ω_1 (ω_3) is given from $\hbar\omega_{12}$ corresponding to the (coherence-) state $|1\rangle\langle 2|$ occupied during t_1 (t_3). The states can be read out of double sided Feynman diagrams. Note that some of the indicated positions correspond to more than one diagram.

Electronic 2D spectra represent the highest level of information that can be achieved in third order optical spectroscopy, as all three intervals t_1 , t_2 and t_3 are resolved. All other third order techniques yield projections or slices of electronic 2D spectra. As 2D-ES signals hold absorptive (real) and dispersive (imaginary) components (see section 2.1.7), the full information content of 2D-ES is only accessible if the two contributions are separated. To do so the electric signal-fields have to be recovered with their appropriate phase from the intensities measured by the photo detector (compare section 2.2.4).

Theory

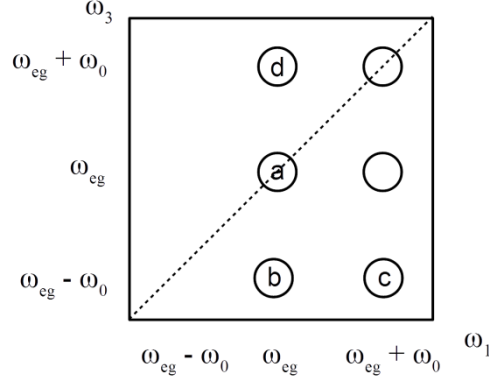


Figure 5. Schematic 2D – spectrum. Labeled circles indicate signals corresponding to diagrams drawn in Figure 1. **a**: Figure 1a with $e = e_0$, $g = g_0$, **b, c, d**: Figure 1b left -, center-, right diagram. $\omega_0 = \omega_{e_0 e_1} = \omega_{g_0 g_1}$

2.2.2 Transient Grating spectroscopy

Just as 2D-ES, Transient Grating (TG) spectroscopy is a FWM technique involving the excitation of a sample with three pulses of different wavevectors (see Figure 4). The only difference to the 2D-ES experiment is that t_1 is not scanned but fixed to $t_1 = 0$. Therefore, ω_1 is not resolved and TG spectra represent slices through the 2D-ES signal $E_{sig}(t_1, t_2, \omega_3)$ at $t_1 = 0$ along ω_3 and projections of $E_{sig}(\omega_1, t_2, \omega_3)$ onto ω_3 (projection slice theorem, see section 3.5.2). More precisely, for finite pulses TG spectra are equivalent to t_1 - integrals of $E_{sig}(t_1, t_2, \omega_3)$ over the pulse duration.

The signals measured in the phase matched direction $k_{sig} = -k_1 + k_2 + k_3$ hold absorptive and dispersive contributions. In analogy to 2D-ES, the absorptive part of the electric signal field can be recovered by heterodyne detection (Het-TG).

2.2.3 Pump Probe spectroscopy

The Pump probe (PP) experiment is illustrated in Figure 6. It involves the excitation of the sample with only two non-collinear ultrashort pulses, the second of which (*probe*) is chosen to be much weaker than the first one (*pump*). Commonly, PP is interpreted by means of two consecutive absorption events with the second pulse probing the molecular system some time t_2 after the irradiation with the pump. Nonlinear response theory (which we employ), however, interprets it differently.

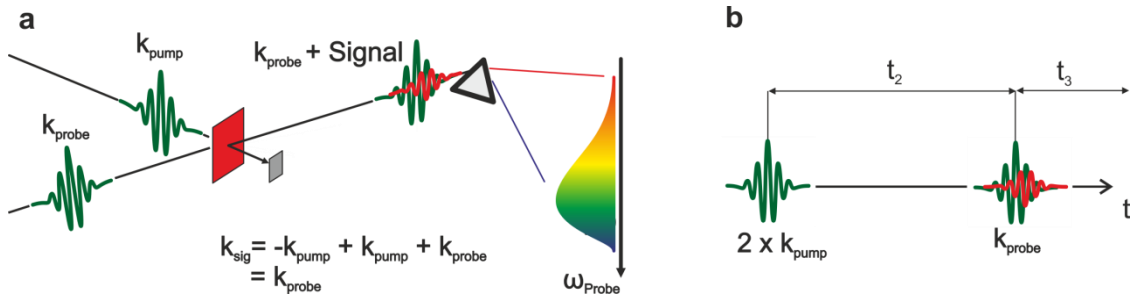


Figure 6. **a**: Illustration of the Pump probe experiment. The pump pulse along k_{pump} excites the sample (red square section). The probe pulse along k_{probe} carrying the signal is measured after being transmitted through the excited sample in absence and presence of the pump pulse. **b**: Time ordering in PP. Adapted from [36] with permission of the authors.

Theory

The relation to the so far presented theory, double sided Feynman diagrams and FWM experiments is established by realizing that the signals measured in PP are produced by two interactions with the pump pulse and a third interaction with the probe pulse. The sequence of interactions is therefore identical to TG (and 2D-ES). However, from the phase matching condition Eq.(2.26), the third order signal's wave vector is given by k_{probe} and the corresponding third order signal co-propagates with the probe as well as first order signals (see Figure 6). Therefore one measures the sum of signal- (first and third order) and probe fields. The third order signal $E_{sig}^{(3)}(t_1=0, t_2, \omega_3)$ is recovered by separately measuring the probe transmitted through the sample with the pump pulse on ($I_{probe}(t_2, \omega_3)$) and off ($I_{probe}^{(0)}(\omega_3)$) and calculating

$$\Delta T(t_2, \omega_3) = \frac{E_{sig}^{(3)}(t_1=0, t_2, \omega_3)}{\sqrt{I_{probe}^{(0)}(\omega_3)}} = \frac{I_{probe}(t_2, \omega_3)}{I_{probe}^{(0)}(\omega_3)} - 1. \quad (2.29)$$

Herein we introduced the transient transmission $\Delta T(t_2, \omega_3)$, which is the most common representation of pump probe signals.

As the first two interactions happen simultaneously ($t_1 = 0$), ω_1 is not resolved. It can be shown that the PP spectrum is equivalent to the projection of the real part of the 2D-ES signal field onto the ω_3 - axis. [35] As will be discussed later this finding is extremely useful. It states that PP signals are purely absorptive.

2.2.4 Heterodyne detection – recovering absorptive and dispersive signal fields

Separation of absorptive and dispersive contributions is achieved by a technique called *heterodyning*. [37] Heterodyning is a well-established technique in various fields of electrical engineering, such as telecommunications, and optical detection. The common element in all applications is the mixing of a signal with a reference signal of known frequency, amplitude and phase, the so called *local oscillator* (LO). In the context of nonlinear spectroscopy heterodyning refers to the mixing of the signal field E_{sig} with a delayed, weak replica of the excitation pulse k_3 , yielding an interferogram I_{int} . If the two co-propagate, i.e. they possess a common wave vector, their interferogram measured at the detector can be written as [38]

$$I_{int}(\omega_3) = (E_{sig}(\omega_3) + E_{LO}(\omega_3)) \times c.c. = I_{sig}(\omega_3) + I_{LO}(\omega_3) + 2\sqrt{I_{sig}(\omega_3)I_{LO}(\omega_3)}\cos(\omega_3 t_{LO}). \quad (2.30)$$

Herein we introduced t_{LO} as the delay between the third pulse k_3 and the LO (see

Figure 5). If the intensity $I_{LO}(\omega_3)$ and phase $\omega_3 t_{LO}$ of the field E_{LO} are known the complex field $E_{sig}(\omega_3)$ can be recovered from the measured interferogram $I_{int}(\omega_3)$. To do so one has to isolate the oscillating term by picking the contributions centred around $t_3 = t_{LO}$ in the t_3 domain after Fourier

Theory

transformation. After shifting the signal to $t_3 = 0$ in a process called *phasing* (compare section 3.5.2), inverse Fourier transformation and division by $\sqrt{I_{LO}}$ the complex signal field is retrieved.

2.3 Vibrational signatures in electronic spectroscopy

The study of vibrational degrees of freedom in electronic spectra of molecules was pioneered by FRANCK [16] and CONDON [17] and developed tremendously by, amongst others, the work of HERZBERG, who wrote on the topic in a series of textbooks entitled *Molecular spectra and molecular structure* [39].

One of the most widely applied principals in the study of vibrational signatures in electronic spectra is the Franck-Condon (FC) principle. We will briefly review this principle based on HERZBERG's work [15,39] as we will invoke it in the interpretation of vibrational signatures in time resolved electronic spectra in chapter 5. We will then apply it to the displaced harmonic oscillator model which we will use to explain the experimental findings of section 4.4.

2.3.1 Vibrational progressions

When an electronic transition is coupled to a vibrational mode of the molecule one observes a so-called vibrational progression of the electronic transition in electronic spectra. The electronic transition at ω_{eg} is accompanied by different quanta Δv of change in vibrational quantum number v . Additional peaks at

$$\omega = \omega_{eg} + \Delta v \times \omega_0 \quad (2.31)$$

show up in electronic spectra. The situation is illustrated by the term diagram shown in Figure 7.

In absorption spectra Δv is usually positive for typical vibrational frequencies ω_0 because higher lying vibrational levels on the electronic ground state are not populated at room temperature. This is indicated in Figure 7 by dotted lines. In steady state emission spectra (fluorescence emission) mainly progression peaks of negative Δv are observed because most excited state population is in the vibrational ground state due to rapid vibrational population relaxation. In ultrafast spectroscopy the timescales of vibrational population relaxation are well resolved and pathways including electronically excited states with $v > 0$ have to be taken into account. If more than one vibrational mode is linked to an electronic transition each vibrational quantum number v_i gives rise to a progression and Eq.(2.31) reads

$$\omega = \omega_{eg} + \sum_i \Delta v_i \times \omega_{0,i} . \quad (2.32)$$

In the electronic/vibronic spectra all possible permutations of Δv_i contribute.

Theory

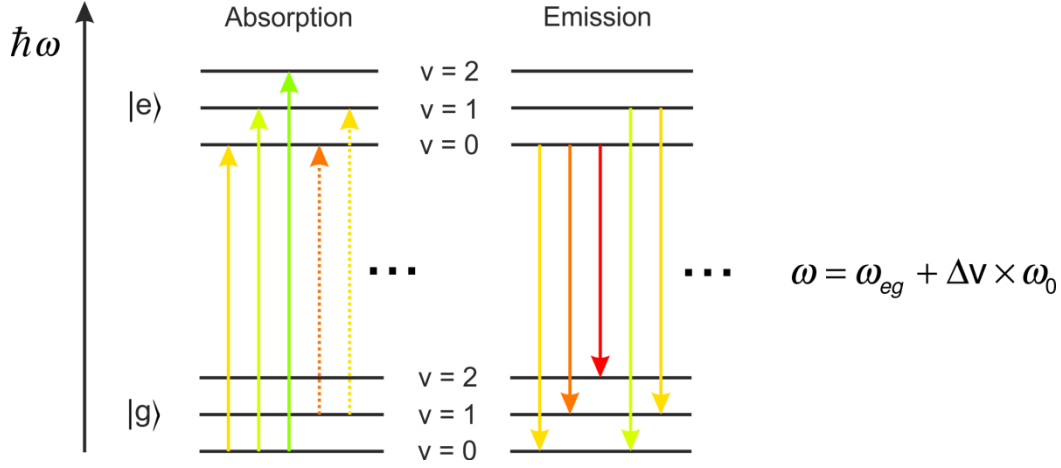


Figure 7. Term diagram of a vibrational progression of an electronic transition. In accordance to spectra of hypericin, the arrows' colours correspond to the colour of light of frequency ω with $\lambda_{eg} = 590 \text{ nm}$ and $\omega_0 = 1300 \text{ cm}^{-1}$.

2.3.2 The Franck-Condon principle, Franck-Condon factors

In the so far discussion of vibrational progression we did not include the probability of the transitions. The magnitude of the signals of a progression can most often be explained by the FC principle, which will be discussed in this section.

To describe spectra including vibrational degrees of freedom one has to turn to a quantum mechanical description of the molecular system that involves electronic coordinates τ_e and nuclear coordinates τ_v . The system's wavefunction can be written in a product-ansatz of the form

$$|\Psi\rangle = |\Psi_e(\tau_e, \tau_v)\Psi_v(\tau_e, \tau_v)\rangle. \quad (2.33)$$

The Franck-Condon principle rests on two assumptions: firstly, the nuclear motion is assumed much slower than electronic motion; therefore the electrostatic potential that the nuclei experience due to the electrons around them is a quasi-static average over the rapidly fluctuating electron density. The nuclear wavefunction Ψ_v is then independent from the electronic coordinates τ_e , $|\Psi_v\rangle = |\Psi_v(\tau_v)\rangle$ (*Born-Oppenheimer approximation*). Secondly, the variation of the electronic wavefunction with the nuclear coordinates is assumed small, i.e. $|\Psi_e\rangle = |\Psi_e(\tau_e)\rangle$ (*Condon approximation*).

To analyse the intensity of signals corresponding to a vibrational progression we calculate the transition dipole moment of a transition $|\Psi'\rangle \rightarrow |\Psi''\rangle$ as

$$\begin{aligned} \mu_{\Psi'\Psi''} &= \langle \Psi' | \mu | \Psi'' \rangle = \\ &= \langle \Psi'_e(\tau_e) \Psi'_v(\tau_v) | \mu_e(\tau_e) | \Psi''_e(\tau_e) \Psi''_v(\tau_v) \rangle + \langle \Psi'_e(\tau_e) \Psi'_v(\tau_v) | \mu_v(\tau_v) | \Psi''_e(\tau_e) \Psi''_v(\tau_v) \rangle \end{aligned} \quad (2.34)$$

Herein we rewrote the dipole operator μ (see. Eq.(2.1)) as a sum of a dipole operator μ_e depending solely on electronic coordinates τ_e and an operator μ_v depending solely on nuclear coordinates τ_v . This allows us to rewrite the second term of Eq.(2.34) as

Theory

$$\left\langle \Psi_v' \left| \mu_v \right| \Psi_v'' \right\rangle \times \left\langle \Psi_e' \left| \Psi_e'' \right\rangle = 0. \quad (2.35)$$

The expression is zero due to the orthogonality of the eigenstates $\left| \Psi_e' \right\rangle$ and $\left| \Psi_e'' \right\rangle$. The transition dipole moment becomes

$$\mu_{\Psi' \Psi''} = \left\langle \Psi_e' \left| \mu_e \right| \Psi_e'' \right\rangle \times \left\langle \Psi_v' \left| \Psi_v'' \right\rangle. \quad (2.36)$$

The first factor in Eq.(2.36) is the electronic transition dipole moment. It is a constant number for all transitions of a progression. The second term is the overlap integral of the vibrational wavefunctions of the initial and final state and is referred to as *Franck-Condon factor*. The FC principle therefore states that the relative intensities of a progression only depend on nuclear wave functions, which are given from nuclear potential energy surfaces. Next, we will analyse the nuclear wave functions of a displaced harmonic oscillator.

2.3.3 The displaced harmonic oscillator

The displaced harmonic oscillator model [39] comprises two harmonic potentials, one on the electronic ground state and one on the electronic excited state, of the form

$$V(r) = V_e + \frac{1}{2}k(r - r_{eq})^2 = V_e + 2\pi^2\omega_0^2m(r - r_{eq})^2. \quad (2.37)$$

The curves are illustrated in Figure 8 a. V_e is a (quasi-)constant electronic potential that defines the frequency of the purely electronic transition. k is a force constant, m is the reduced mass of the oscillator. Note that we switched to the normal mode coordinates r from the general nuclear coordinates τ_v (see normal modes [40]). k and r_{eq} are in general different in the electronic ground- and excited state. The effect of different force constants k is usually small and is neglected hereafter. If the differences in k are small the vibrational wavefunctions are identical in the electronic ground and excited state, except for a shift in the vibrational coordinate r by $d = r_{eq}' - r_{eq}''$. The FC factor in Eq.(2.36) can then be expressed as

$$\left\langle \Psi_v' \left| \Psi_v'' \right\rangle = \left\langle \Psi_v^m(r) \left| \Psi_v^n(r - d) \right\rangle =: FC_{m,n}. \quad (2.38)$$

The superscripts m, n in $FC_{m,n}$ refer to the vibrational quantum number in the “non-displaced ground state” and the vibrational quantum number in the “displaced excited state.”

The eigenfunctions of the time-independent Schrödinger equation for the potential given in Eq.(2.37) are the Hermite orthogonal functions. [39]

$$\Psi_v^m(r) = \frac{\text{Hermite}_m(r) \times \exp(-r^2/2)}{\sqrt{2^m m! \sqrt{\pi}}} \quad (2.39)$$

Theory

Herein, $\text{Hermite}_m(r)$ denotes the m^{th} - order Hermite polynomial in r . Eq.(2.39) and Eq.(2.38) fully explain, amongst others, the intensities of progression peaks of the displaced harmonic oscillator in linear, but also nonlinear spectra. They will form the basis for the discussion of vibrational coherences in the time resolved spectra presented in this work. To this end, two properties of the FC-factors of the displaced harmonic oscillator are given.

$$\text{FC}_{m,n} = \text{c.c.}(\text{FC}_{m,n}) = \langle \Psi_v^m(r) | \Psi_v^n(r-\delta) \rangle = \langle \Psi_v^n(r-\delta) | \Psi_v^m(r) \rangle \quad (2.40)$$

$$\text{FC}_{m,m+1} = -\text{FC}_{m+1,m} = \langle \Psi_v^m(r) | \Psi_v^{m+1}(r-\delta) \rangle = -\langle \Psi_v^{m+1}(r) | \Psi_v^m(r-\delta) \rangle \quad (2.41)$$

The first equality states that Eq.(2.39) is real valued and the FC factors for absorption and emission events are equal for a given pair of states. The second equality arises from the $(-1)^n$ - symmetry of the n^{th} - Hermite polynomial towards inversion. [41]

In linear absorption and fluorescence spectra, the intensity of peaks scales with the square of the transition dipole moment and therefore the square of FC factors. For the peaks of a vibronic progression from a vibrational ground state it can be shown [24] that the intensities are given by a Poisson distribution in the vibrational quantum number v :

$$I(\omega \pm v\omega_0) \sim \left| \langle \Psi_v^0 | \Psi_v^v \rangle \right|^2 \sim \exp(-D) \frac{D^v}{v!} \quad (2.42)$$

Herein we introduced the Huang-Rhys factor $D = d^2 m\omega_0/2\hbar$. The Poisson distribution Eq.(2.42) is plotted in Figure 8 **b** for two values of D .

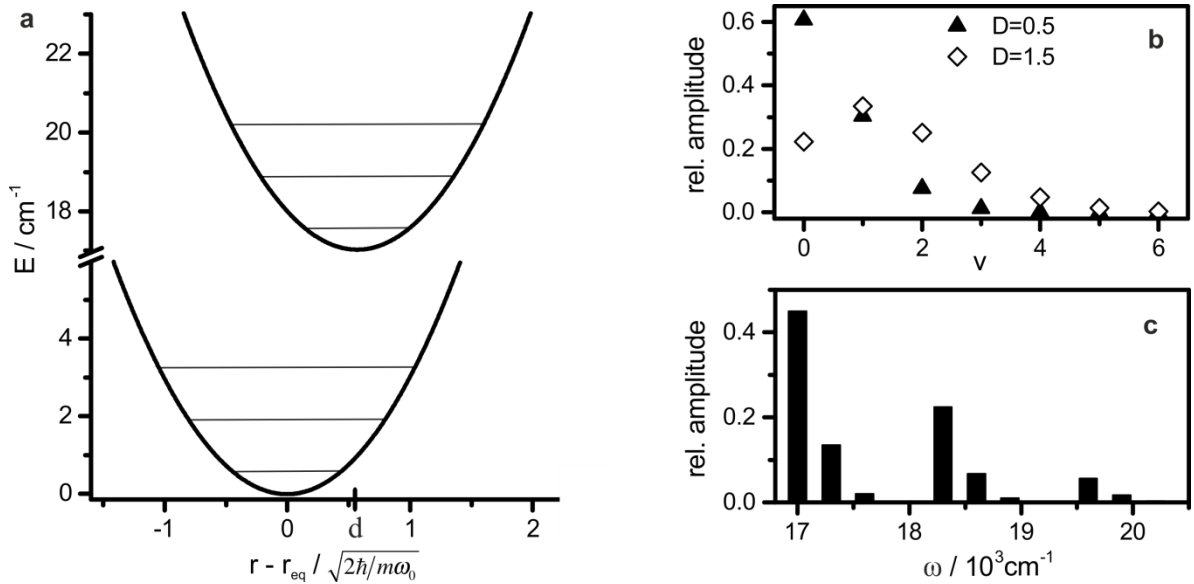


Figure 8. **a**: Harmonic potentials on electronic ground and excited state, displaced by d . $\omega_{\text{eg}} = 17000 \text{ cm}^{-1}$, $\omega_0 = 1300 \text{ cm}^{-1}$. **b**: Poisson distributions Eq.(2.42) for $D = 0.5$ and $D = 1.5$. **c**: Stick spectrum of a progression of an electronic transition $\omega_{\text{eg}} = 17000 \text{ cm}^{-1}$ by two harmonic potentials $\omega_0^{v1} = 1300 \text{ cm}^{-1}$, $\omega_0^{v2} = 300 \text{ cm}^{-1}$, $D^{v1} = 0.5$, $D^{v2} = 0.3$.

Theory

When a linear molecular spectrum is influenced by multiple normal vibrational modes the amplitudes of the progression are described by a multi-dimensional Poisson distribution

$$\langle \Psi_v^0 | \Psi_v^v \rangle \sim \prod_i \exp(-D_i) \frac{D_i^{v_i}}{v_i!}. \quad (2.43)$$

v_i is the vibrational quantum number and D_i the Huang-Rhys factor of the i^{th} mode. The frequency of the corresponding peak is given by Eq.(2.32). A progression of two normal modes is illustrated in Figure 8 c.

3 Experimental

The first three sections of this chapter describe the laser setup and optics used for the experiments. The preparative procedures as well as the procedures of recording steady state Raman, fluorescence and absorption spectra and time resolved 2D-ES, Het-TG and PP spectra will be described in section 3.4. Section 3.5 will cover data processing and analysis of time resolved spectroscopic data, finishing with a model used to extract relevant parameters from the steady state absorption spectrum.

3.1 Pulse generation and compression

In this section the laser system used for all nonlinear experiments is briefly outlined. Techniques employed to shorten the pulses' duration, *i.e.* *pulse compression*, are described.

Broadband ultrashort pulses were generated in a home built non collinear optical parametric amplifier (NOPA) [42] described in [43]. Herein, a white light *signal* pulse is amplified by mixing it with a ~ 400 nm *pump* pulse in a β -Barium-Borate crystal. The amplified spectrum can be tuned as described in [43]. Both, the pump and the white light signal are generated from ultrashort pulses produced by a Coherent RegA laser system. The latter consists of a Mira Seed modelocked ultrafast laser, a RegA Model 9050 amplifier laser and a Verdi V-18 pump laser. The modelocked laser [44] is a Ti:sapphire solid state laser [45] producing ultrashort pulses of approximately 20 fs centred at 790 nm. These are amplified by the regenerative amplifier laser (also Ti:sapphire) [46] at a repetition rate of 60 kHz. Both lasers are pumped by a diode-pumped frequency doubled Nd:YVO₄ laser, emitting 18 W of 532 nm CW - light.

To provide pulses near the transform limit it was necessary to compensate for dispersion $d^j n/d\lambda^j$ of different order j picked up throughout the pulse generation and the optical path through the experiment [47] [48]. In the nonlinear experiments described below two techniques of compression were used: *prism pair compression* [49] [50] and a setup similar to the so called $4f$ - *shaper* [48]. The prism compressor was a standard prism pair setup, consisting of two fused silica prisms placed into the beam path at Brewster's angle θ_B (Figure 9, **a**). In this setup, the incident beam passes through the prisms and is dispersed. A mirror is placed behind the second prism at 90° in the paper plane, but slightly tilted upwards. After reversing the path through the prisms the beam is picked up by a mirror just above the incident beam (out of paper plane in Figure 9, **a**). The path between the prisms is longer for blue light. By varying the position of the second prism as indicated in Figure 9 group velocity dispersion $d^2 n/d\lambda^2$ could be compensated. The $4f$ - setup is depicted in Figure 9, **b**. The incident beam is dispersed in the paper plane by a grating. The grating is placed in the focus of a cylindrical mirror of focal length f . The second, identical cylindrical mirror, placed at a distance of $2f$ from the first one, focuses the collimated beam onto a second grating which recombines the dispersed colours. The overall optical path length of $4f$ gives the setup its name. In the ideal configuration described, the setup does not affect the beam and functions as a retroreflector. Most commonly the system is used to manipulate the beam's spectrum in the Fourier plane (the mirror symmetry plane in Figure 9, **b**),

Experimental

where each colour is focused into one point [48]. In our application it was not used like that, but instead slightly detuned to optimize the beam's profile and pulse width. Most importantly, the beam's spatial chirp, *i.e.* the spectrally inhomogeneous beam profile, in the direction normal to the paper plane in Figure 9 was corrected by slightly rotating the gratings around their surface normal as indicated.

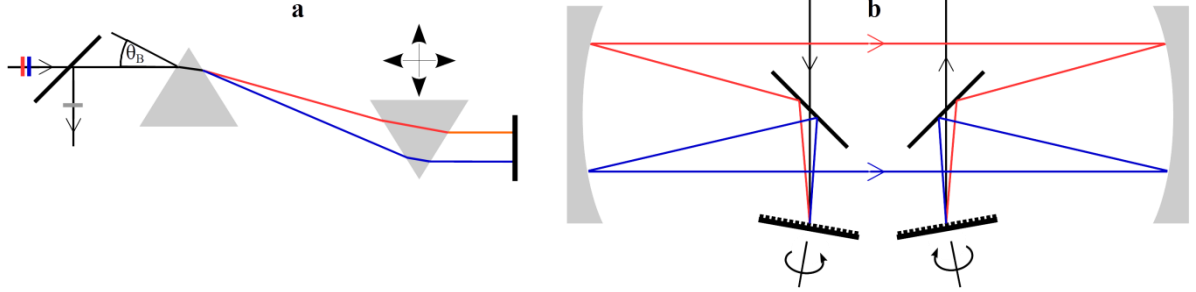


Figure 9. Pulse compression (schematic). See text. **a**: Prism pair setup. **B**: 4f-setup.

3.2 Pulse characterization

Characterization of the excitation pulses was carried out at the sample position. The power of the pump beams (k_1 , k_2 , k_3) was measured to 0.7 mW each, corresponding to pulse energies of 12 nJ. Their common focus in the sample cell was approximately 85 μm in diameter, resulting in a photon flux of $5 \times 10^{13} \text{ cm}^{-2}$ per pulse. The pulses spectra were centred at 585 nm with a FWHM of approximately 60 nm (Figure 10, right).

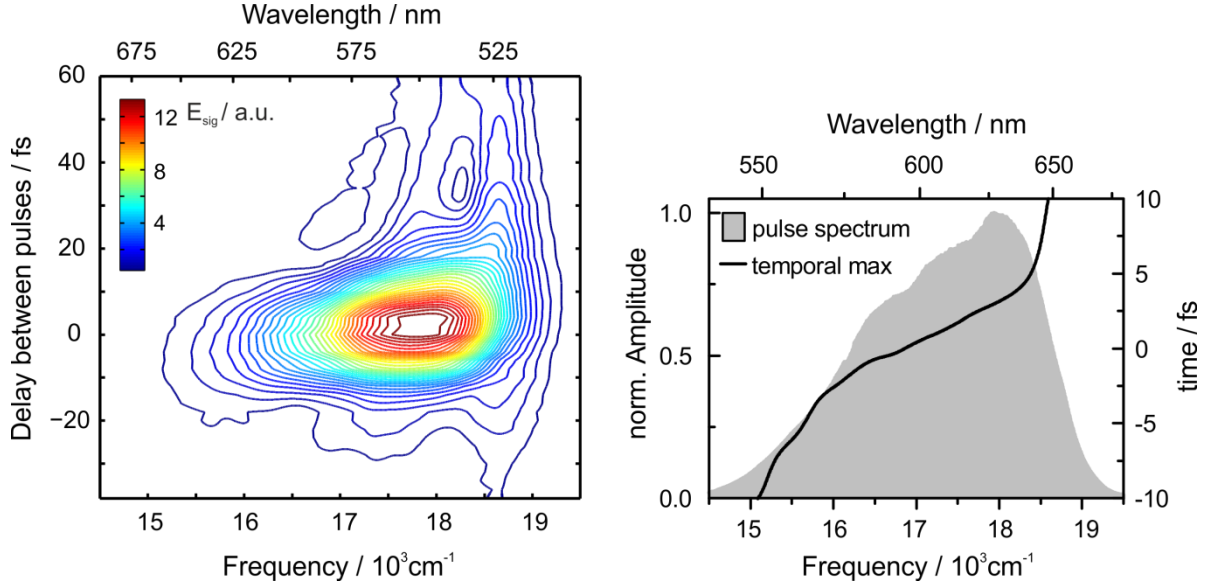


Figure 10. Representative example of pulse spectra. Left: FROG trace recorded in neat water. Right: Spectrum of the excitation pulses (grey area) and time of maximum FROG-signal as determined from a Gaussian fit to the FROG traces for each frequency (*chirp*).

The pulses' temporal profile was measured in frequency resolved optical gating (FROG) experiments [51]. FROG traces were recorded by measuring the so called coherent artefact in water, *i.e.* the signal measured when setting $t_1 = 0$ and scanning t_2 around $t_2 = 0$ in a TG setup (see below). From this method a temporal FWHM of 17 fs was measured, varying by approximately 4 fs between

Experimental

different experiments. By fitting a Gaussian profile along t_2 for every frequency to the FROG traces the temporal maximum was found to vary with the frequency, *i.e.* the excitation pulses were slightly positively chirped (red before blue, see Figure 10, right). Reducing this chirp and the temporal FWHM of the pulses *via* the prism pair without losing spectral bandwidth was subject to an almost daily optimization procedure and carried out with best effort. Figure 10 represents a compromise between bandwidth and chirp.

The phase stability between pulses was measured to $\lambda/60$ in previous experiments [52] for pulses generated at common diffractive optical elements (k_1 and k_2 ; k_3 , LO+ and LO-; see Figure 11). This is essential for the recording of optical frequencies (ω_l) in the time domain (t_l) and for stable heterodyning of the TG signals. The stability between k_2 and k_3 was not measured but has to be considered significantly worse than $\lambda/60$ because these pulses do not run over common reflective optics. This results in path length fluctuations on the order of the amplitude of the mirrors' vibrations. Since only slowly oscillating signals with wavelengths much bigger than the mirrors' vibrations are measured during t_2 the results presented below are not corrupted.

3.3 Experimental apparatus

All nonlinear measurements presented below were carried out using the same setup. TG and 2D-ES use identical optical settings while PP requires only minor adaptations described below. Note that the described setup is only one of many possible implementations of 2D-ES. For a review of other implementations see [53].

3.3.1 2D-ES and Het-TG

The setup is described in [52] and its scheme is reprinted from [52] in Figure 11 with permission of the authors. In essence it facilitates the splitting of the incident pulse into five, the introduction of scanable delays between them as well as their focussing into the sample cell. For convenience we will denominate the three pulses facilitating the third order signals after their wave vector (k_1 , k_2 , k_3). The beam coming from the pulse compression section is split 50:50 at a beamsplitter (BS). The transmitted beam, that will form k_3 and the LOs, is retroreflected by two mirrors mounted at 90° . The mirrors are mounted on a computer controlled linear precision stage that is used to introduce the delay t_2 ($1 \text{ fs} \cong 0.15 \text{ } \mu\text{m}$ of stage movement).

Both, the transmitted and the reflected beam, are guided into diffractive optical elements (DOE) placed in the focal point of spherical mirrors (SM). One DOE generates k_1 and k_2 from the non-delayed beam. These run atop of each other in Figure 11. Similarly, the beam delayed by t_2 passes through a second DOE that produces an intense k_3 - beam and the two LOs (LO+ and LO-) with an intensity of approximately 1% of k_3 . k_1 , k_2 and k_3 pass through pairs of wedged fused silica plates (WP). One of the wedges forming WP2 is mounted on another precision stage moving linearly in a direction perpendicular to the beam. Thereby the amount of glass in the beam path of k_2 is varied and the delay t_l is introduced. WP1 and WP3 are static and solely compensate for dispersion. All beams

Experimental

travel parallel as they approach SM3. Before SM3 the beams are transmitted through glass plates of different thickness. Thereby, the delays between k_3 and the LOs is introduced such that the LOs precede the pump pulses. A cross section of the parallel running beams is given in inset (A) of Figure 11. SM3 focuses the beams into a common point in the sample where the signal is generated. The parts of the signal emitted in the phase matched direction $-k_1 + k_2 + k_3$ (compare section 2.1.5) copropagate with LO+ and interference occurs. The interferogram of the signal and LO+ is spectrally dispersed by a grating spectrometer and imaged onto the CCD - camera's pixel array. A calibration links the horizontal pixel position of the camera to ω_3 .

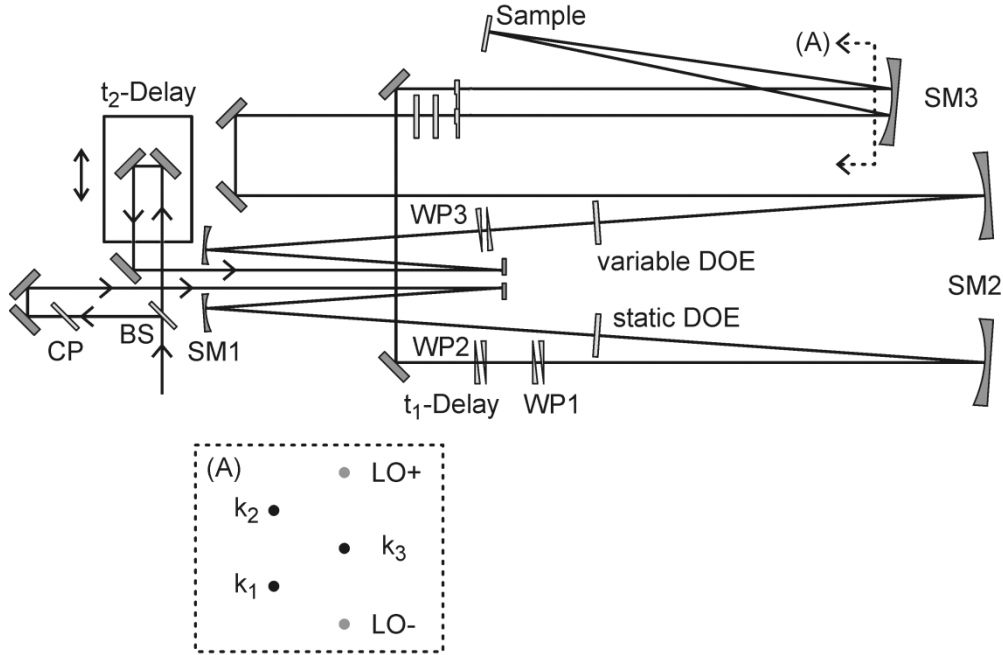


Figure 11. Optical setup for 2D-ES, TG and PP experiments. BS: Beam splitter; CP: compensation plate; SM: spherical mirror; WP: wedge pair; DOE: diffractive optics element. Reprinted from [52]

3.3.2 Pump Probe

To adjust the described setup to a PP configuration the pump pulses k_1 and k_3 are blocked. k_2 serves as the pump and LO+ as the probe which is recorded by a CCD – camera as described above, while the delay between k_2 and LO+ is scanned *via* the t_2 - delay line.

3.4 Experimental procedures

3.4.1 Sample preparation

The sample, hypericin primary reference standard, was purchased from HWI Analytik GmbH. A saturated solution in ethylene glycol, spectrophotometric grade, was prepared by sonicating the solution at approximately 40 °C and isolating the clear dark red supernatant after centrifuging. The resulting stock solution was diluted for the different experiments to give the desired optical density (OD) of 0.55 at a path length of one centimetre in absorption and fluorescence measurements and 0.2 at a path length of 200 μm in nonlinear measurements (OD given for $\lambda = 596 \text{ nm}$). All solutions were

Experimental

stored in the dark and degassed with Argon repeatedly to avoid photo oxidation of hypericin by singlet oxygen known to be formed from hypericin's triplet state [54].

For all time resolved spectroscopic measurements the sample was introduced in the focus of M3 (Figure 11) in a 200 μm flow cell from Hellma Analytics and circulated at approximately 1 mL/min. The flow cell was chosen over the usually employed freely flowing film in a wire-guided drop jet [55] to keep the sample under an inert, oxygen free atmosphere and avoid photo oxidation. Flow cells are avoided due to the possibility of nonlinear signals from glass and additional scatter contributions, as will be discussed in chapter 4.

3.4.2 Pump Probe spectroscopy

The PP scanning routine is described as follows: Before every scan of t_2 the pump was blocked and the spectra of LO+ and LO- were recorded ($I_{probe}^{(0)}$, $I_{ref}^{(0)}$). LO- was recorded throughout the scans as a reference to balance the spectra for variations of the laser power. This is possible because LO- carries no third order signal since it does not overlap with the pump pulse in the sample. Next the LOs were blocked and the scatter of the pump was measured (I_{scat+} , I_{scat-}). Finally all beams were unblocked and spectra of the two LOs, with LO+ carrying the third order signal, were recorded for the desired values of t_2 ($I_{probe}(t_2)$, $I_{ref}(t_2)$). The scans were repeated numerous times to improve the signal to noise ratio. For the PP spectrum presented in section 4.2 (Figure 15) t_2 was scanned from -100 fs to 800 fs in steps of 9.3 fs. The scan was repeated 50 times. All spectra were sampled onto 2048 data points (the camera's horizontal resolution) ranging from 379.7 THz to 624.9 THz.

The recording of a spectrum took approximately 2.5 s per t_2 - step. The integration time of the camera was set to approximately 100 ms to run it at $\sim 80\%$ of saturation to minimize read out noise. The power of the LOs was set to the rather unusually high value of 1 % of the pump to amplify the signal relative to the very large contributions of scatter discussed below.

3.4.3 2D Electronic Spectroscopy and Heterodyned Transient Grating

As discussed above Het-TG is exactly equivalent to the 2D-ES experiment with the only difference being that t_1 is not scanned but fixed to zero. Throughout the experiments LO- and all co-propagating signals were blocked behind the sample position. Before every scan the spectrum of LO+ ($I_{LO}(\omega_3)$) was measured with all other beams blocked. Next all beams (except for LO-) were unblocked and the interferogram of signal and LO+ was recorded for the desired range of t_2 ($I_{int}(t_2, \omega_3)$).

For the 2D-ES spectrum discussed in section 4.3 (Figure 16) only a single value of $t_2 = 156$ fs was recorded. t_1 was scanned ten times from -200 fs to 200 fs in steps of 1.33 fs ($I_{int}(t_1, t_2, \omega_3)$). As this sampling does not fulfil the Nyquist criterion for optical frequencies around 500 THz ($\tau = 2$ fs) these frequencies are undersampled. The process of retrieving undersampled frequencies is discussed in section 3.5.3.

Experimental

For the Het-TG spectra shown below t_1 was fixed to zero. $t_1 = 0$ was found by setting $t_2 = 1$ ps and scanning t_1 . The point of maximum signal intensity defined $t_1 = 0$. Spectra were recorded for t_2 ranging from -248.2 fs to 2250.2 fs in steps of 8.00(3) fs. The scan was repeated 82 times with alternating scan direction to avoid effects of long time drifts, such as slowly decaying laser power, which would show up in the spectra as a decay along t_2 if one only scanned with positive t_2 increments.

The intensity of LO+ in both experiments was chosen via a variable neutral density filter to be approximately 60 times bigger than the signal (at $t_1 = 0$), resulting in a modulation depth of 12 %, i.e. the amplitude of the oscillating term in Eq.(2.30) was 12 % of the sum of the non oscillating terms.

3.4.4 Steady state experiments

The resonant Raman spectrum presented below was recorded on a Witec alpha 300 RAS+ confocal Raman microscope. In contrast to all other measurements presented in this text the sample (Hypericin primary reference standard) was measured in its solid state because the Raman intensities of the dissolved samples were too low. The sample was prepared on a CaF₂ window and excited with 1 mW of 532 nm radiation.

Absorption and fluorescence spectra were recorded with a resolution of 1 nm. Fluorescence emission was measured with an excitation wavelength of 547 nm. Due to the very small stokes shift the fluorescence and absorption spectra of hypericin overlap, resulting in reabsorption of fluoresced light within the cuvette. This was compensated for [56] by calculating a corrected spectrum $I_{cor}(\lambda)$ from the recorded spectrum $I_{rec}(\lambda)$ using

$$I_{cor}(\lambda) = I_{rec}(\lambda) \times \frac{-\ln(10^{-OD(\lambda)})}{1 - 10^{-OD(\lambda)}}. \quad (3.1)$$

3.5 Data Processing and Analysis

All data processing described below was carried out in MATLAB. The described functions refer to MATLAB functions.

3.5.1 Pump Probe

From the above described spectra the pump probe signal was calculated as

$$\Delta T(t_2) = \frac{\langle (I_{probe}(t_2) - I_{scat+}) / (I_{ref}(t_2) - I_{scat-}) \rangle}{\langle I_{probe}^{(0)} / I_{ref}^{(0)} \rangle} - 1 \quad (3.2)$$

Herein, $\langle \rangle$ denotes the averaging operation over all scans. This equation represents an extension of Eq.(2.29) to include balanced detection and subtraction of pump scatter (compare section 3.4.2 for a definition of variables in Eq.(3.2)). A detailed analysis of different balancing schemes can be found in [57].

Experimental

3.5.2 Data processing of Het-TG and 2D-ES; phasing

As discussed in section 2.2, signals measured in Het-TG and 2D-ES experiments can be real (absorptive) or imaginary (dispersive). The aim of the processing steps described below is to extract and separate these contributions from the interferograms $I_{\text{int}}(t_1, t_2, \omega_3)$.

The process of separating the heterodyne interferogram into real and imaginary signals is outlined for Het-TG in Figure 12. We will start the discussion with Het-TG, as Het-TG is always included in any 2D-ES experiment, and afterwards discuss the adaptations necessary for 2D-ES.

In a first step the spectrum $I_{LO}(\omega_3)$ recorded before each scan was subtracted from the interferograms $I_{\text{int}}(t_2, \omega_3)$. Next all consecutive scans were averaged. For the Het-TG spectra presented below only 54 out of the 82 recorded scans were averaged because some spectra were corrupted by too low Laser power or by significant scatter contributions. The averaged scans were Fourier transformed along ω_3 to $I_{\text{int}}(t_2, t_3)$ using the *ifft* - function. In the t_3 - domain the oscillating term of Eq.(2.30) was isolated by applying a single sided Gaussian window function centred at $t_3 = 0.742$ ps with a FWHM of 0.184 ps (Figure 12, centre). After Fourier transform from t_3 back to ω_3 using the *fft* - function the complex valued spectra $I(t_2, \omega_3)$ were multiplied by $\exp(i\omega_3 t_{LO}) / \sqrt{I_{LO}}$ to shift the signal to $t_3 = 0$ in the t_3 domain and to arrive at the complex signal field. Although this sounds straight forward the last step is challenging because t_{LO} has to be known to a precision of at least $\tau / 50$ to correctly separate real and imaginary components. [29] This corresponds to 33 attoseconds for $\omega_3 = 500$ THz. t_{LO} cannot be measured directly with this precision and slightly varies on a day to day basis. Therefore t_{LO} had to be determined in a process called phasing via a fitting routine. [29] This step makes use of the equality of the real part of the TG signal and the PP signal explained in section 2.2.3. [35] During phasing the residuals

$$\Delta T(t_2, \omega_3) \times \sqrt{I_{\text{probe}}(\omega_3)} - C \times \Re(E_{TG}(t_2, \omega_3, t_{LO})) \quad (3.3)$$

of the phased real TG signal and a beforehand measured PP spectrum were minimized in a least square sense by varying t_{LO} and C (compare Eq.(3.2) and Eq.(2.29)). Herein, $\Re(E_{TG}(t_2, \omega_3, t_{LO}))$ denotes the real part of the transient grating signal calculated using t_{LO} . C is a constant scaling factor. Because of the high noise level in PP and the absence of fast dynamics along t_2 a single value of t_{LO} was determined for all t_2 from PP and TG spectra averaged over a t_2 - range from 100 - 800 fs.

Before all steps described above 2D-ES spectra $I_{\text{int}}(t_1, t_2, \omega_3)$ were Fourier transformed to $I_{\text{int}}(\omega_1, t_2, \omega_3)$ and integrated over all ω_1 , yielding the projected spectrum $I_{\text{int}}(t_2, \omega_3)$. The step of Fourier transforming the undersampled spectrum is discussed below. The projected spectra were treated equivalently to the above described Het-TG spectra. In doing so we assumed that the projected 2D-ES spectrum and the TG spectrum are equal. This assumption is true because of the so called projection slice theorem. [58] The projection slice theorem states that, for a given two dimensional function, the Fourier transform of a projection of the function onto one dimension is the same as a slice through the Fourier transform

Experimental

along the same dimension through the origin. The Het-TG spectrum is a slice through the 2D-ES spectrum along the ω_3 axis at $t_1 = 0$ and therefore the projection slice theorem applies. Note that in principle one could find t_{LO} by simply picking the spectrum $I_{int}(t_1=0, t_2, \omega_3)$ from the 2D-ES data set. The projection of the Fourier transformed data however gives more reliable results.

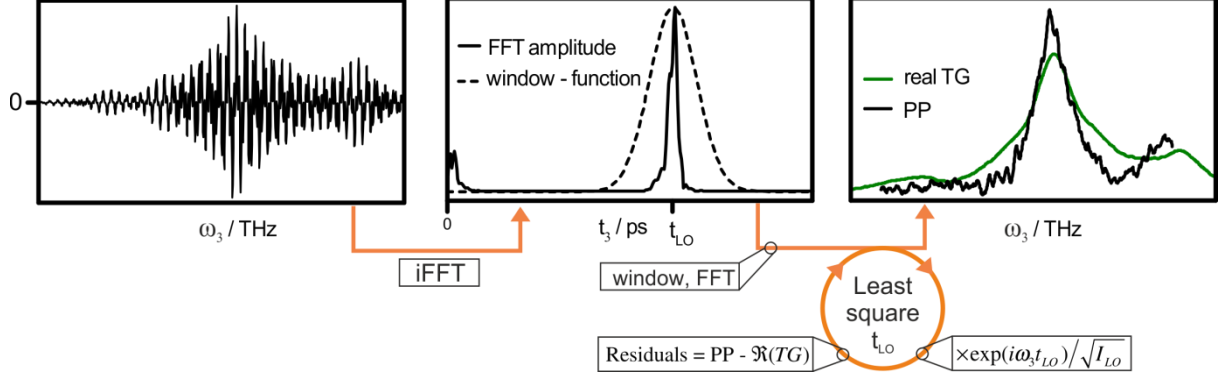


Figure 12. Phasing. Left: Interferogram of LO and signal field excluding constant contributions. Centre: Interferogram in t_3 – domain after inverse Fourier Transform and Gaussian window function used to isolate the signal. Right: Pump probe (PP) and phased real Transient Grating (TG) spectrum.

3.5.3 Further analysis of 2D-ES

As discussed above the spectra were undersampled along t_1 . This is a popular method in 2D-ES because it reduces the large number of data points that have to be sampled and therefore allows one to acquire more scans and increase signal to noise ratio. The process is described in [29] for 2D - infrared spectroscopy. Undersampled signals appear at aliasing frequencies

$$\omega = \omega_0 - m\omega_N \quad (3.4)$$

in the Fourier spectrum. Herein, ω_0 is the original signal frequency, ω_N is the Nyquist frequency corresponding to half the sampling frequency and m is an odd integer. The signal was extracted from the $m = 3$ aliasing frequency component centred around -250 THz using a boxcar window. The frequency-axis was corrected using Eq.(3.4) with $m = 3$.

The second step in the analysis of 2D-ES data after phasing was the separation of rephasing and non-rephasing signals. This was achieved by separating the dataset into $I_{int}(t_1 > 0, t_2, \omega_3)$ and $I_{int}(t_1 < 0, t_2, \omega_3)$ (compare Figure 2, R_1 and R_2). Finally, the value of t_{LO} found in the phasing process was used to calculate the real and imaginary components of the rephasing and non-rephasing signals.

3.5.4 Analysis of vibrations in Heterodyned Transient Grating

The Transient Grating spectra were analyzed for their vibrations along t_2 (compare section 4.4.1). In this section we will describe how the ω_3 - resolved vibrational amplitudes and phases discussed below were extracted from the Het-TG spectra. The procedure is outlined in Figure 13.

In a first step the spectra's population dynamics were modeled by *global analysis* (GA) using a sequential model with two time constants. [59] GA was performed using MATLAB code developed by JASPER VAN THOR, LUUK VAN WILDEREN and CRAIG LINCOLN described in [60]. Via this step the slowly varying signal contributions could be subtracted from the data to isolate the oscillating parts of

Experimental

the signal. In essence, GA models time resolved spectra by considering the two dimensional map to be a superposition of a number of spectral species, called *decay associated spectra* (DAS). The coefficients of the spectra are time dependent, forming time traces. Their temporal evolution is given by a user defined model. The two dimensional data set is described by a matrix product of the DAS – matrix and the time traces – matrix (Figure 13, **b**, Eq.(3.7)). For the Het-TG scan shown in Figure 17 (results), two time constants and DAS were sufficient to describe the coherent artefact and population dynamics. Global analysis was performed including data from $t_2 = -20$ to 2250 fs and $\omega_3 = 14679 \text{ cm}^{-1}$ (440 THz) to 18678 cm^{-1} (560 THz).

The residuals from the global fit were Fourier transformed along t_2 for each detection frequency in the range $t_2 = 0.104$ to 2.146 ps and then summed over all detection frequencies. The resulting projected Fourier power spectrum was plotted (Figure 18) and the frequencies of the five most intense peaks were used as initial guess parameters in the following step. The resolution in ω_2 is 15 cm^{-1} .

To retrieve the magnitude and phase of each oscillation we employed GA on the residuals of the first GA. The time traces, rather than being rate equations (as in the description of population dynamics in the first GA), took the form of exponentially damped cosines and sinusoids.

$$Trace_{\cos,i}(t_2) = \exp(-t_2/\tau_i) \times \cos(\omega_{2,i}t_2) \quad (3.5)$$

$$Trace_{\sin,i}(t_2) = \exp(-t_2/\tau_i) \times \sin(\omega_{2,i}t_2) \quad (3.6)$$

Herein, τ_i is the damping constant and $\omega_{2,i}$ is the frequency of the i^{th} mode. The corresponding DAS were calculated using the *mldivide* function to solve the system of linear equations

$$\begin{pmatrix} DAS_{\cos,1}^{\omega_{3,1}} & DAS_{\sin,1}^{\omega_{3,1}} & \cdots & DAS_{\cos,5}^{\omega_{3,1}} & DAS_{\sin,5}^{\omega_{3,1}} \\ \vdots & \vdots & \ddots & \vdots & \vdots \\ DAS_{\cos,1}^{\omega_{3,1002}} & DAS_{\sin,1}^{\omega_{3,1002}} & \cdots & DAS_{\cos,5}^{\omega_{3,1002}} & DAS_{\sin,5}^{\omega_{3,1002}} \end{pmatrix} \cdot \begin{pmatrix} Trace_{\cos,1}^{t_{2,1}} & \cdots & Trace_{\cos,1}^{t_{2,269}} \\ Trace_{\sin,1}^{t_{2,1}} & \cdots & Trace_{\sin,1}^{t_{2,269}} \\ \vdots & \ddots & \vdots \\ Trace_{\cos,5}^{t_{2,1}} & \cdots & Trace_{\cos,5}^{t_{2,269}} \\ Trace_{\sin,5}^{t_{2,1}} & \cdots & Trace_{\sin,5}^{t_{2,269}} \end{pmatrix} = \begin{pmatrix} residuals(\omega_3, t_2) \end{pmatrix} \quad (3.7)$$

Herein, the coordinates along ω_3 and t_2 are given as superscripts $\omega_{3,i}$ and $t_{2,i}$. The parameters τ_i and ω_i were fitted in a least square sense using the residuals defined by

$$residuals_{GA2} = residuals_{GA1} - \sum_{i=1 \dots 5} DAS_{\cos,i}(\omega_3) \cdot Trace_{\cos,i}(t_2) + DAS_{\sin,i}(\omega_3) \cdot Trace_{\sin,i}(t_2). \quad (3.8)$$

Subscript *GA1* denotes residuals from the first GA.

From the cos- and sin- spectra the amplitudes A_i and phases φ_i of the oscillations were calculated as

$$A_i(\omega_3) = \sqrt{DAS_{\cos,i}^2(\omega_3) + DAS_{\sin,i}^2(\omega_3)} \quad (3.9)$$

$$\varphi_i(\omega_3) = \arctan\left(\frac{DAS_{\sin,i}(\omega_3)}{DAS_{\cos,i}(\omega_3)}\right). \quad (3.10)$$

Phase jumps of 2π were corrected using the *unwrap* function.

Experimental

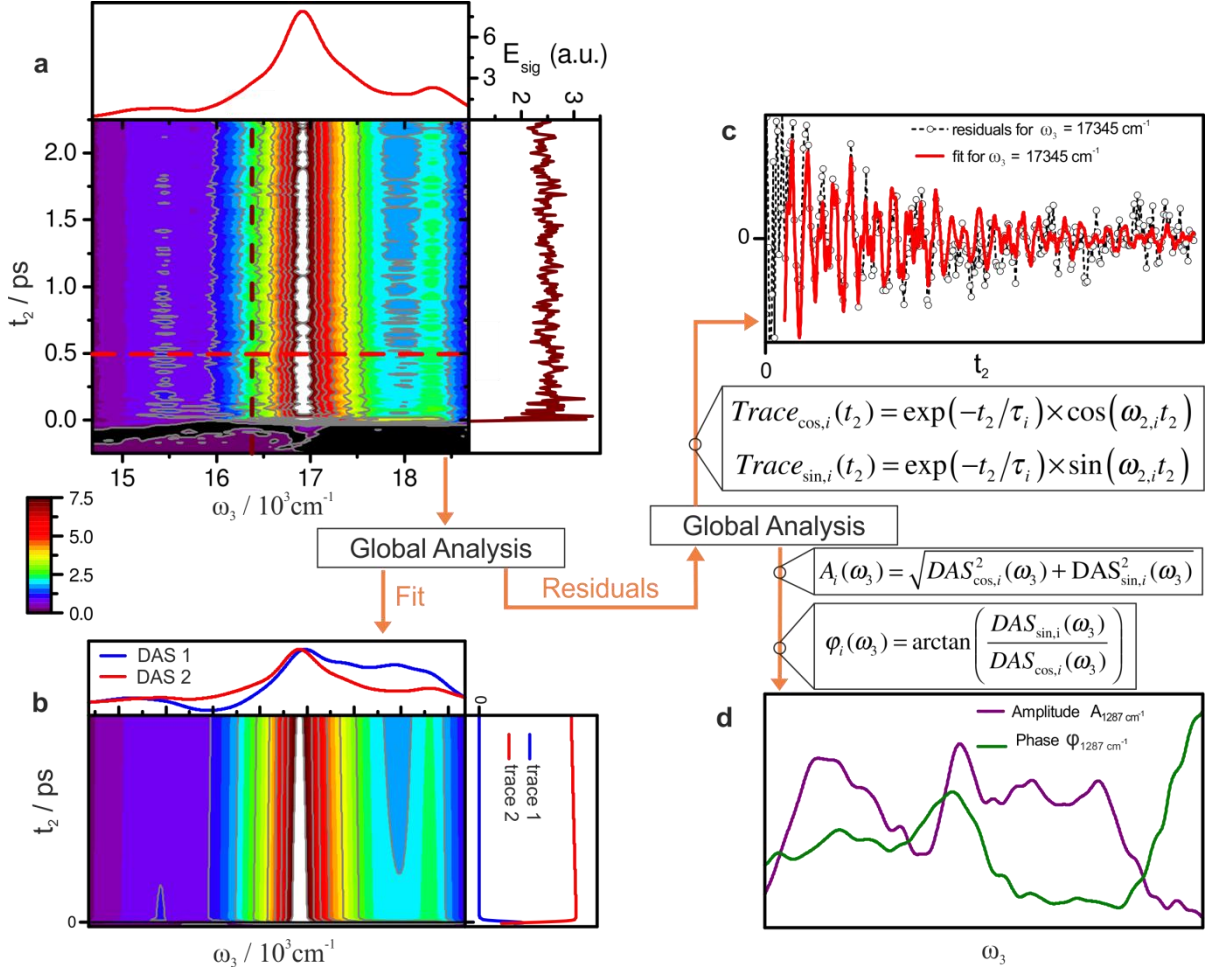


Figure 13. Data processing of the phased data for the extraction of oscillatory amplitudes and phases. (a) Map of real TG spectra and slices along ω_3 (top panel) and t_2 axis (right panel) at indicated positions (dashed lines). (b) Result of global analysis. Top panel: decay associated spectra (DAS); right panel: corresponding time traces; (c) Residuals of global analysis for $\omega_3 = 17345 \text{ cm}^{-1}$ and global fit of five exponentially decaying oscillators; (d) Amplitude and phase of the 1287 cm^{-1} oscillation.

Evaluation of the presented method of retrieving the phase and amplitude of oscillations is presented in Appendix B. Additionally, the results are compared with a more common analysis based on fast Fourier transform with eight-fold zero padding [61].

3.5.5 Model for fitting of hypericin's absorption spectrum

The absorption spectrum shown in Figure 14 (results) was fitted using a displaced harmonic oscillator model based on the theory presented in section 2.3. The model describes the spectrum by means of two electronic transitions, one of which, centred around 17000 cm^{-1} , is subject to progressions of two vibrational harmonic modes. The second electronic transition at approx. 21000 cm^{-1} is fitted by a single Gaussian profile. The twelve model parameters are listed and described in Table 1. The model function f is given by Eq.(3.11)-(3.14). $G(\mu, \sigma)$ denotes a Gaussian profile, $L(\mu, \Gamma)$ a Lorentzian profile and P_a^b a Poisson distribution in a , defined by the Huang-Rhys factor D_b (compare Eq.(2.42)).

$$f = B \times G(\mu_B, \sigma_B) + A \times \sum_{j=0, \dots, 2} \sum_{k=0, \dots, 2} P_j^1 P_k^2 \times ((1-w)G(\mu_A - j\nu_1 - k\nu_2, \sigma_A) + wL(\mu_A - j\nu_1 - k\nu_2, \Gamma)) \quad (3.11)$$

Experimental

$$G(\mu, \sigma) = \frac{1}{\sigma\sqrt{2\pi}} \exp\left(-\frac{(x-\mu)^2}{2\sigma^2}\right) \quad (3.12)$$

$$L(\mu, \Gamma) = \frac{1}{2\pi} \frac{\Gamma}{(x-\mu)^2 + 0.25 \times \Gamma^2} \quad (3.13)$$

$$P_a^b = \exp(-D_b) \frac{D_b^a}{a!} \quad (3.14)$$

Table 1. Parameters of the displaced harmonic oscillator model used to fit hypericin's absorption spectrum

Parameter	Description	Parameter	Description
A, B	scaled transition dipole moments	w	Shape factor. 0 ... Gauss, 1 ... Lorentz
μ_A, μ_B	Electronic transition frequency	ν_1, ν_2	Frequency of harmonic oscillator
σ_A, σ_B	Gaussian width	D_1, D_2	Huang – Rhys factor
Λ_A	Lorentzian width		

4 Results

In this chapter we present and discuss steady state and ultrafast optical spectra of hypericin. Steady state spectra presented in section 4.1 show clear signatures of vibrational progression, as confirmed by the fit of the absorption spectrum by a displaced harmonic oscillator model. Pump probe and 2D-ES spectra presented in sections 4.2 and 4.3 suffered from strong scatter. Although the same was true for Het-TG, a spectrum could be recorded *via* this technique that even resolved relatively weak oscillatory signals (section 4.4). Their amplitudes and phases will be discussed in great detail in chapter 5.

Note that, in accordance to common practice in literature of 2D-ES, ω refers to ordinary frequency in the figures and their discussion below, in spite of its use as a circular frequency in the equations presented in this text.

4.1 Steady state spectroscopy

The absorption spectrum and a fluorescence emission spectrum, recorded at an excitation wavelength $\lambda_{ex} = 547$ nm, are depicted in Figure 14. The spectra are dominated by the electronic singlet transition from the electronic ground state to the first excited state, $S_0 \rightarrow S_1$, centred at 16900 cm^{-1} / 592 nm. This transition is assigned to the first $\pi \rightarrow \pi^*$ transition with a transition dipole moment parallel to the C_2 axis of hypericin (horizontal in Figure 14) [62]. The electronic transition is subject to two clearly visible vibrational progressions. The high frequency progression is comprised of several closely spaced modes at approx. 1240 cm^{-1} , 1300 cm^{-1} and 1375 cm^{-1} while two low frequency modes at approx. 440 cm^{-1} and 300 cm^{-1} show up as shoulders on the high frequency progression peaks (see also Figure 18). The second $\pi \rightarrow \pi^*$ transition's dipole moment ($S_0 \rightarrow S_2$) is aligned perpendicular to the first one [62] and its energy corresponds to 21100 cm^{-1} / 473 nm.

Figure 14 additionally shows the fitted model function described by Eq. (3.11). The fitted parameters are given in Table 2. The fit was carried out in OriginPro 2015G. The model was fitted to 350 data points from 12000 cm^{-1} to 22170 cm^{-1} . The high energy region of the spectrum, especially the $S_0 \rightarrow S_2$ – peak, is poorly described due to additional electronic transitions other than $S_0 \rightarrow S_2$ and their progressions that could not be included in the model.

Results

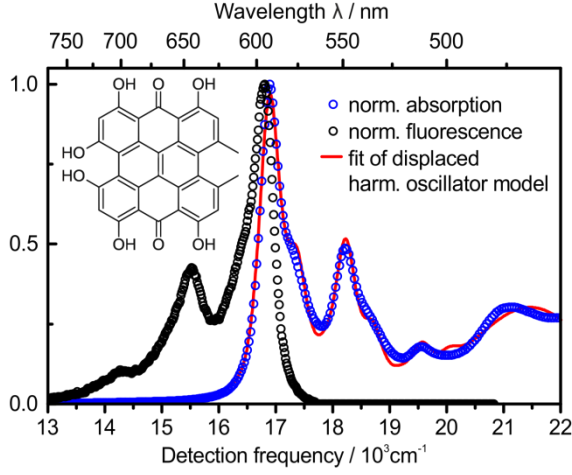


Figure 14. Normalized absorption- and fluorescence emission spectra ($\lambda_{ex} = 547$ nm) of hypericin (inset) in ethylene glycol.

Table 2. Fitted parameters of model Eq.(3.11)

Parameter	Value	Parameter	Value
A / cm^{-1}	1299(8)	Γ / cm^{-1}	430(20)
B / cm^{-1}	764(16)	w	0.64(3)
μ_A / cm^{-1}	16893(19)	v_1 / cm^{-1}	1333(3)
μ_B / cm^{-1}	21480(20)	v_2 / cm^{-1}	474(5)
$\sigma_A / \text{cm}^{-1}$	184(8)	D_1	0.495(5)
$\sigma_B / \text{cm}^{-1}$	1030(20)	D_2	0.395(8)

4.2 Pump Probe spectroscopy

Pump probe spectroscopy of hypericin proved challenging. Especially scatter contributions from the sample itself and from the glass windows hampered the data quality significantly. During the experiments, portions of the sample aggregated at the windows where the beams hit the sample, causing additional scatter. In an attempt to solve the problem the cell was slightly moved up or down roughly every thirty minutes.

Although scatter spectra were recorded before each scan and subtracted from each spectrum in accordance to Eq.(3.2), a complete removal of scatter contributions was not possible in this straight forward manner. The interference pattern of the probe and scatter from the pump could not be removed from the signal because it cannot be recorded separately in absence of signal (*i.e.* in absence of the pump). The pattern is clearly visible at early t_2 times in the PP-map shown in Figure 15, left. In the t_3 / t_2 representation (Fourier transformed along ω_3 , Figure 15, right) the pattern shows up at $t_3 = t_2$. For $t_2 > 100$ fs the interference pattern was digitally removed in the t_3 - domain by applying a rectangular window function around $t_3 = t_2$.

The PP spectra are dominated by GSB and SE signals at 16900 cm^{-1} referring to the $S_0 \rightarrow S_1$ transition and the GSB of the first vibrational progression peak at approximately 18200 cm^{-1} . On the low energy side the expected SE peak of the vibrational progression at $\omega_3 \approx 15500 \text{ cm}^{-1}$ is not observed. Besides the high noise level the significantly lower power of the excitation pulse at the red spectral end may explain this finding (compare Figure 10).

The overall data quality of the PP spectra did not allow for a comprehensive analysis of the spectra for subtle spectral dynamics or vibrations along t_2 . We therefore limit ourselves to the analysis of Het-TG spectra presented below as they hold, after phasing, identical information as PP spectra.

Results

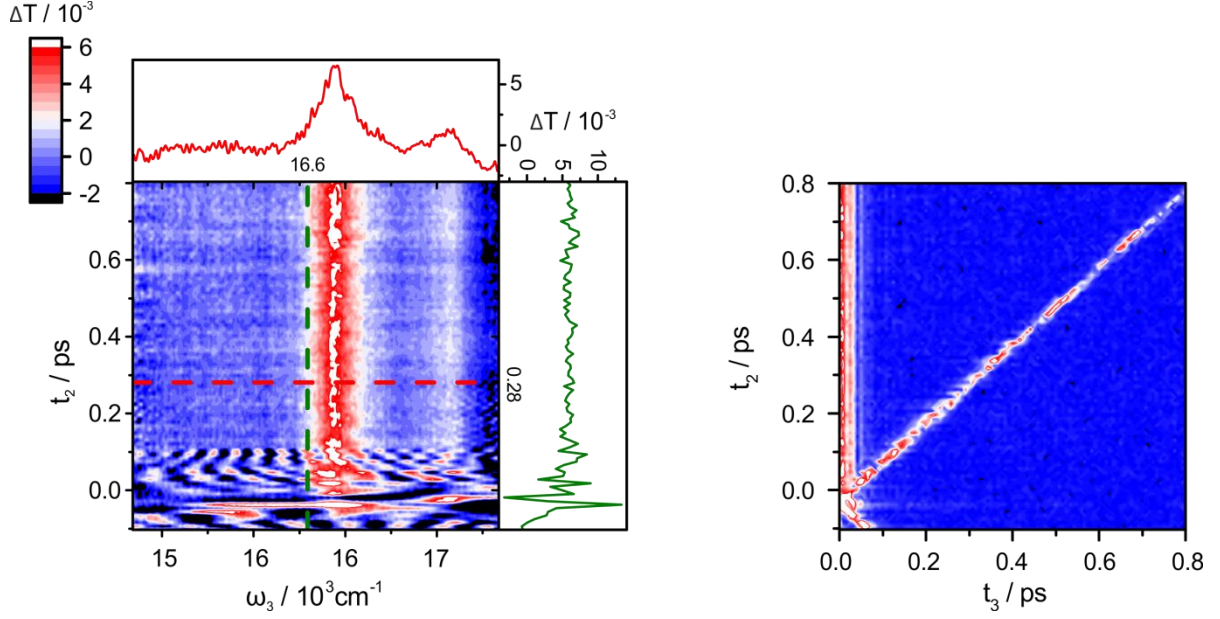


Figure 15. Left: Pump probe scan of hypericin in ethylene glycol. Scatter contributions were removed for $t_2 > 0.1$ ps (see text). Right: Unfiltered pump probe scan in the t_3 domain. Scatter of the pump interfering with the probe is clearly visible at $t_3 = t_2$.

4.3 2D-ES

The above mentioned problems related to scatter persist for 2D-ES with the additional difficulty of much longer scan times and correspondingly smaller numbers of scans that could be averaged. For this reason and due to the lack of significant dynamics in the PP – and Het-TG – spectra (see below) t_2 was not scanned but fixed to 156 fs. The phased total (rephasing + nonrephasing) 2D-ES map is shown in Figure 16. A detailed discussion of the spectrum is again precluded by the poor signal to noise ratio. The spectrum illustrates, however, the expansion of ω_3 in an additional dimension, the excitation frequency ω_1 . Some examples of double sided Feynman diagrams contributing to the spectrum as well as their positions in ω_1 / ω_3 are given in Figure 16. Expected peaks centred at $\omega_3 \approx 15600 \text{ cm}^{-1}$ are again missing.

Results

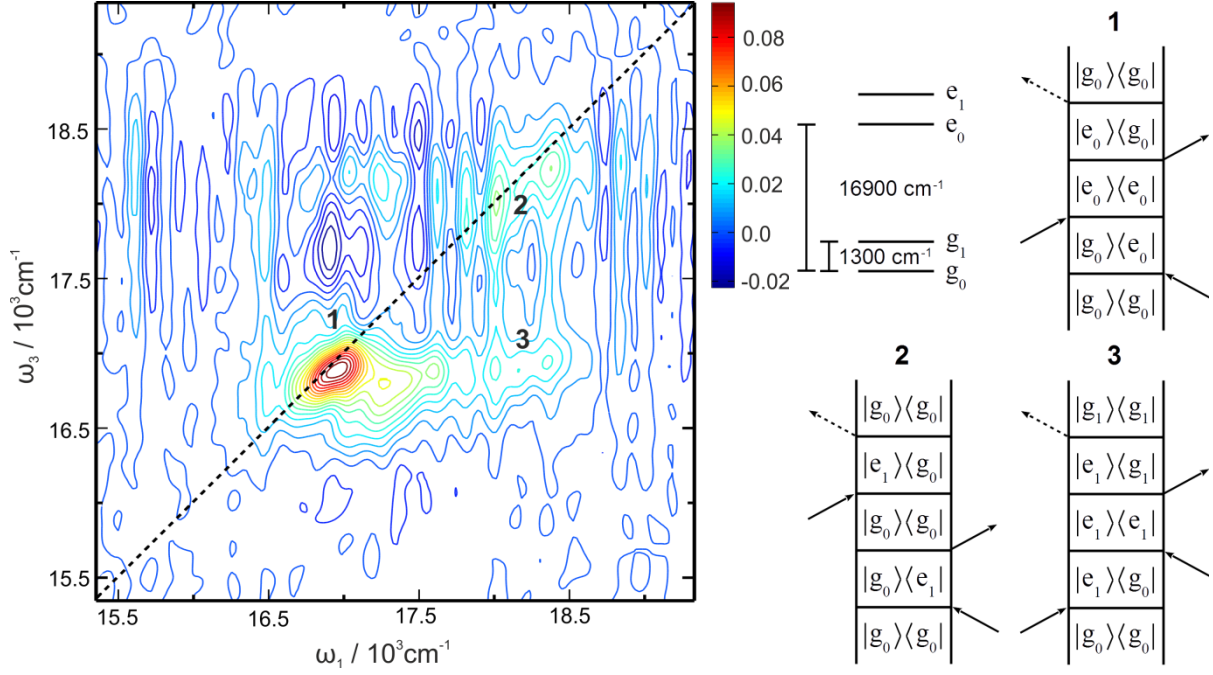


Figure 16. Total phased 2D-ES map of hypericin at $t_2 = 156$ fs and examples of double sided Feynman diagrams contributing to it. **1**: Rephasing stimulated emission, **2**: Rephasing ground state bleach, **3**: Non rephasing stimulated emission.

4.4 Het-TG

The Het-TG spectrum shown in Figure 17 as well as Het-TG scans up to $t_2 = 30$ ps are qualitatively similar to the steady state absorption and fluorescence spectra shown in Figure 14. The vibronic progression peaks discussed above for the steady state spectra are clearly visible on both, the high and low energy side of the electronic transition frequency of 16900 cm^{-1} . The low energy band that could not be observed in PP or 2D-ES could be resolved in Het-TG, yet it is still relatively weak compared to the high energy band. When assuming that the model of a displaced harmonic oscillator applies and that no dynamic processes influence the spectra it is expected that the time resolved spectra are largely similar in shape to the steady state spectra. A possible cause for the deviation from this expectation is the low power of the excitation pulses at the red end of the spectrum (Figure 10). Global analysis of t_2 population dynamics found a time constant of ~ 70 ps, *i.e.* much greater than our scan ranges. Besides this slow population dynamics, no significant spectral dynamics were observed.

Results

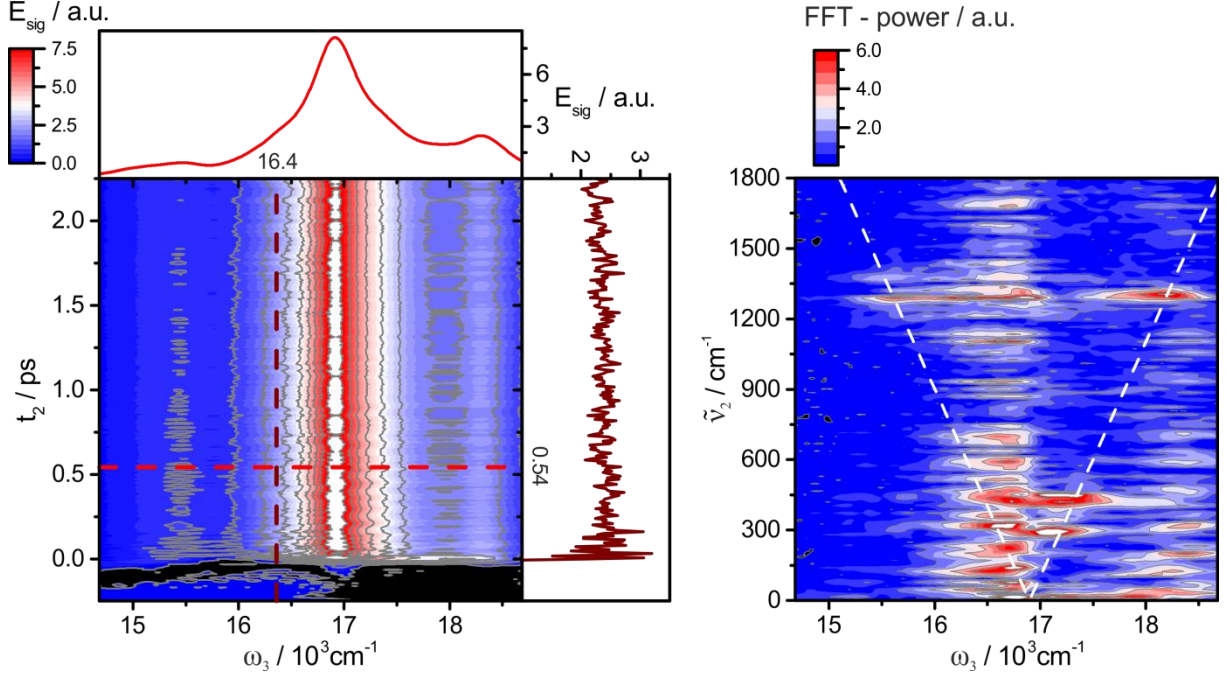


Figure 17. Left: phased real Het-TG map of hypericin. Top and right panels show slices through the map at indicated positions. Right: Absolute FFT – amplitude (FFT - power) map of the residuals of a global fit to the map shown on the left hand side (see text). The FFT is taken from 0.1 ps to 2.25 ps without zero padding (269 datapoints). White dashed lines drawn at $\tilde{\nu}_2 = |16900 \text{ cm}^{-1} - \omega_3|$ indicate expected peak positions $\omega_3 = \omega_{eg} + \Delta\nu \times \omega_0$ corresponding to vibrational progressions of $\Delta\nu = \pm 1$ (compare Eq.(2.32)).

4.4.1 Vibrations in Het-TG spectra

The residuals of global analysis include, besides noise, signals that oscillate along t_2 at the frequency of molecular vibrations, *i.e.* signals from *vibrational coherence (VC) states*. These signals are resonant Raman (RR) signals, and spectroscopic techniques aiming at the recording of these signals in the time domain are referred to as *impulsive Raman spectroscopy*. [61] To analyze VC signals the residuals were Fourier transformed along t_2 (see section 3.5.4). The resulting ω_2 / ω_3 - map is shown in Figure 17. The projection of this map onto the ω_2 axis is shown in Figure 18 and compared to a RR spectrum of the pure, solid hypericin sample. For the three most dominant vibrational contributions in the TG spectrum, centred at 300 cm^{-1} , 440 cm^{-1} and 1290 cm^{-1} , we find corresponding peaks in the RR spectrum as well as in literature [63]. We attribute additional peaks in the RR spectrum at frequencies higher than 1400 cm^{-1} as well as differences in relative amplitudes of peaks to the differing aggregate state of the sample in the two measurements as well as the finite spectrum of the excitation pulses in the TG – experiment. The effect of temporally and spectrally finite excitation pulses will be addressed in section 5.3.2. For an assessment of this aspect a Gaussian fit to the excitation pulses' spectrum is shown in Figure 18 as grey dashed line (compare also Figure 10).

Results

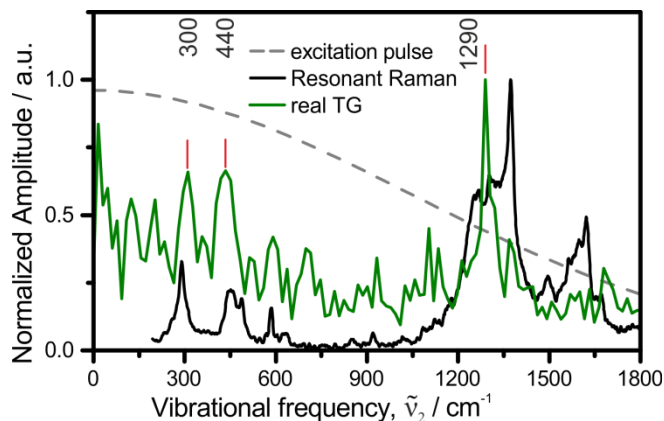


Figure 18. Black line: Resonant Raman spectrum of pure, solid hypericin ($\lambda_{ex} = 532$ nm). Green line: Projection over ω_3 of the Fourier power spectrum shown in Figure 17, right, governed from the phased real Het-TG spectrum of hypericin in ethylene glycol. Grey dashed line: Gaussian fit to the excitation pulse spectrum, shifted to 0 cm^{-1} .

For the analysis of vibrational amplitudes and phases as a function of detection frequency we will limit ourselves to the three most prominent modes centred around 300 cm^{-1} , 440 cm^{-1} and 1290 cm^{-1} . The amplitude - and phase spectra of these modes are plotted for phased, real TG as well as for absolute TG in Figure 19.

We first turn to the real, absorptive part of the TG signal (green lines). The low frequency modes of 300 cm^{-1} and 440 cm^{-1} appear qualitatively similar. Their amplitudes show pronounced dips at the electronic resonance frequency, accompanied by a phase jump of approximately π from low to high detection frequency ω_3 . Their amplitudes peak at or close to the vibronic progression peaks. In contrast, the 1290 cm^{-1} mode shows distinct maxima at the electronic resonance frequency as well as at the vibronic progression peak positions. The amplitude is significantly smaller between the peaks. The phase as extracted from the experiment exhibits a pronounced slope that has to be classified as an experimental artefact (see section 5.3.2). For visualization purposes the phase spectra of the 1290 cm^{-1} mode were straightened by subtracting a linear fit from the original phase spectrum (full lines in Figure 19, 1290 cm^{-1}). A change in phase similar to that found for the low frequency modes can be observed around the centre frequency.

Vibrations in absolute TG (dispersive + absorptive signals) differ from those in the absorptive signals in both amplitude and phase. At the electronic resonance frequency the vibrational amplitude shows no dip as observed in real TG and the phase undergoes no significant change. Analysis of the 1290 cm^{-1} – mode's phase is again hampered by the pronounced slope.

Results

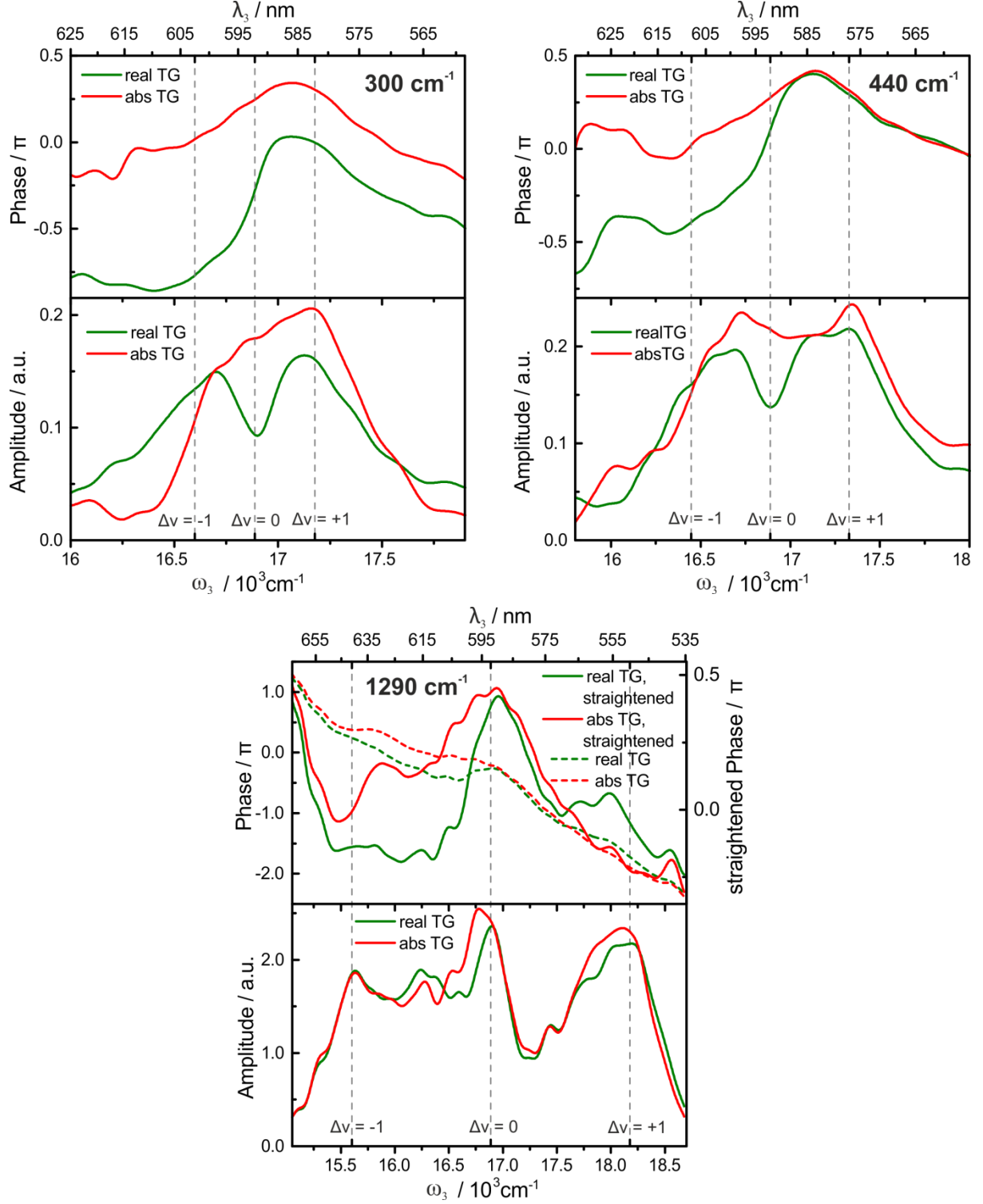


Figure 19. Amplitude - and phase spectra of vibrations in phased real TG and absolute TG for $\tilde{\nu}_2 = 300 \text{ cm}^{-1}$, $\tilde{\nu}_2 = 440 \text{ cm}^{-1}$ and $\tilde{\nu}_2 = 1290 \text{ cm}^{-1}$. Dashed vertical lines indicate the spectral positions of the absorption maximum ($\Delta v = 0$) along with the first vibronic side band positions ($\Delta v = \pm 1$). The retrieved phases of the 1290 cm^{-1} mode (dashed lines) show a significant slope, whose origin is discussed in the text. For visualization purposes, straightened phase spectra (full lines, right-hand y - axis) were calculated by subtracting a fitted straight line from the data.

5 Discussion

In this chapter we discuss the experimental results for Het-TG. All other spectra were discussed in chapter 4. We start with a discussion of advantages of Het-TG over PP that enabled the recording of vibrational spectra (Figure 19) under demanding experimental conditions. In section 5.2 the global analysis approach for retrieving oscillatory signals from time resolved spectra is briefly discussed as it is, to our knowledge, new to the field of ultrafast spectroscopy. The vibrational amplitude- and phase spectra presented in Figure 19 are explained qualitatively in section 5.3.1 by applying the Franck Condon principle to the transition dipole moments in the molecular response function of a displaced harmonic oscillator. To keep the response functions and their interpretation simple we invoke the limit of impulsive excitation (excitation by delta pulses) and neglect effects of finite lineshapes and dispersive signal contributions. Their effects and oscillations in dispersive signals are discussed in sections 5.3.2 and 5.3.3.

5.1 Advantages and experimental aspects of Het-TG in comparison to PP

The results presented in sections 4.2 and 4.4 illustrate the experimental difficulties associated with hypericin and the advantages of Het-TG over PP that enabled the recording of weak vibrational signals. One important advantage is that in TG (and other four wave mixing techniques) signals are recorded background free as they are emitted in a unique phase matched direction. Using PP for impulsive Raman spectroscopy requires the resolution of vibrational modulations of relatively small transient absorptions. Assuming transient absorptions of 10^{-2} - 10^{-3} AU and modulations on the order of 1 - 10 % requires detection limits of 10^{-3} - 10^{-5} AU, which makes the recording of high quality spectra challenging. The vibrational signals in TG can be slightly bigger than in PP because the signals are produced by three intense pump pulses instead of an intense pump and a weak probe as is the case for PP. More importantly, however, they are recorded without large undesired background, which reduces the requirements for a large dynamic range of the detector system.

Significant additional experimental advantages arise when detecting TG - signals in a heterodyned detection scheme. [53,64] Firstly, it enables the recovery of the amplitude and phase of the electric signal field instead of its modulus square (see section 3.5.2). Secondly, as can be seen from Eq.(2.30), heterodyning linearizes the detector signal in E_{sig} and amplifies it by a factor of $\sqrt{I_{LO}}$. To increase the signal to noise ratio the LO intensity is often chosen orders of magnitude ($\sim 10^3$) bigger than the signal itself. The LO, however, also contributes a constant term to Eq. (2.30) that has to be subtracted from the signal. The choice of the ideal ratio I_{LO} / I_{sig} is heavily dependent on the detection system, the intensity of the signal and the sources of noise (constant or proportional in the absolute signal detected). For single point detectors, large LO - intensities can be chosen as the constant I_{LO} - background can be subtracted easily by chopping one of the pump pulses and isolating the modulated signals in a lock-in amplifier [64]. As single point detectors require the recording of an interferogram

Discussion

to resolve ω_3 , which is inherently slow, most modern systems are based on CCD - cameras with ω_3 -dispersed detection in a spectrograph. [53] The limited speed of the camera, however, typically does not allow the rapid acquisition of modulated spectra. This was also the case for our setup. The constant contribution of the LO therefore had to be subtracted in post processing (see section 3.5.2), which limited the feasible ratio I_{LO} / I_{sig} . In latest systems [65] fast (tens of kHz) CCD - cameras are used in combination with choppers to combine the advantages of signal modulation and fast recording of spectra in what is referred to as *shot to shot* or *single shot* detection.

On the downside, compared to PP, TG is more demanding with respect to the optical setup. Most importantly, the phase stability between the first two pulses, and additionally between the third pulse and the LO in heterodyne detection, has to be ensured. The precise spatial overlap of three instead of two pulses in the sample may be an additional source of errors.

5.2 Data analysis, retrieval of vibrational amplitude and phase

Utilizing global analysis in the time domain for the retrieval of vibrational amplitude and phase is, to our knowledge, a new approach not reported on in literature on time resolved spectroscopy. Therefore, a brief discussion of the topic and comparison to the more common techniques of discrete Fourier transformation (DFT) is provided (see Appendix B). Note that time domain fitting procedures are, however, known to metrology literature. [66,67]

The main motivation for turning to an alternative to DFT is its inherent discrete sampling of frequencies. As discussed in section 2.1.7 using Eq.(2.27) and (2.28) the causal nature of the measured signals, *i.e.* the fact that no signal field is emitted before the interaction of the sample with the third excitation field, causes an abrupt jump of the imaginary part of the signals in the frequency domain at the resonance frequency (see Figure 3). As the phase of an oscillation is calculated as $\arctan[\Im(E(\omega))/\Re(E(\omega))]$ it relies critically on the proper sampling of the rapidly changing $\Im(E(\omega))$. This problem is usually addressed by zero padding (see Appendix B). For global analysis ω is not discrete but a continuous fitting parameter, which circumvents this issue. We take care to note that the introduced technique does not overcome principle limitations of Fourier transformation, such as limited spectral resolution imposed by the scanned range. For resolved oscillations fulfilling the model assumptions it will, however, find the frequencies that describe the data in an optimal way and additionally yield physically relevant model parameters, such as dephasing times.

5.3 Analysis of vibrational coherence in Het-TG

The dependence of vibrational phase and amplitude on detection frequency (Figure 19) has been discussed previously in literature using the Wigner phase-space picture of VC, also called the *wavepacket formalism*. [68–72] Here we utilize third order response functions and FC overlap integrals for a displaced harmonic oscillator model introduced in section 2.3. This approach is described in [73] for the molecule Zn-phthalocyanine, whose most important difference to hypericin in

Discussion

the context of the following discussion is that instead of a single electronic excited state two degenerate excited states are dipole accessible in Zn-phthalocyanine.

We will show how FC overlap integrals enter the response functions. A systematic analysis of double sided Feynman diagrams corresponding to VC signals will provide an analytical explanation for experimental findings in Figure 19. In the derivation of this explanation we assume impulsive excitation, *i.e.* all excitation pulses are delta pulses in the time domain, and neglect lineshapes, *i.e.* the molecular response function is assumed to be zero except at the spectral positions of the vibronic progression. The latter simplification limits the validity of the results to absorptive signals (real TG, PP). We will discuss the expected effects of deviations from these assumptions in an attempt to explain the experimental findings made for the 1290 cm⁻¹ mode.

5.3.1 Theoretical predictions for a displaced harmonic oscillator model within the impulsive limit

In order to discuss the oscillatory signals presented above within the context of nonlinear response theory we analyse all VC double sided Feynman diagrams for a system comprising two electronic levels and their first two vibrational levels (see Figure 20). Two vibrational levels are sufficient due to the relatively small curve displacements found in section 4.1. We define VC diagrams as diagrams in which $\rho^{(2)}$ is in a vibrational coherence during t_2 . VC on the excited state, $|e_1\rangle\langle e_0|$ or its complex conjugate, appears in SE pathways and is sometimes referred to as *vibronic coherence* to distinguish it from *vibrational coherence* on the ground state, $|g_1\rangle\langle g_0|$ or c.c., which only appears in GSB pathways. [6] The diagrams are given in Figure 20.

As discussed in section 2.1.3 (Eq.(2.18) - (2.21)) the signal corresponding to a third order diagram scales with the product of four transition dipole moments (sometimes referred to as *the transition dipole product*). Additionally to scaling the signals, the generally complex transition dipole product carries a phase which, together with other parameters, gives the phase of the signal [74]. We can therefore use the transition dipole product to explain vibrational amplitude and phase spectra.

In section 2.3.2 and 2.3.3 the transition dipole moments of a displaced harmonic oscillator within the approximations of the FC principle were analysed and expressed as the product of a purely electronic transition dipole moment μ_{eg} and the FC factor depending on the initial and final vibrational states (Eq.(2.36) and (2.39)). μ_{eg} is equal for all possible transitions in Figure 20 as only two electronic levels are involved. The product of the four FC factors, however, is different for the diagrams depicted in Figure 20. Two examples of transition dipole products are given in Eq.(5.1) and (5.2). Herein, $FC_{m,n}$ denotes the FC factor for a transition from a ground state vibrational wave function Ψ_v^g to an excited state vibrational wave function Ψ_v^e (see Eq.(2.38)) or vice versa (see Eq.(2.40)).

$$SE_R(\omega_{eg}, t_2, \omega_{eg}) \sim \mu_{eg}^4 \times FC_{0,0} \times FC_{0,1} \times FC_{1,0} \times FC_{1,1} \quad (5.1)$$

$$SE_R(\omega_{eg} + \omega_0, t_2, \omega_{eg}) \sim \mu_{eg}^4 \times FC_{0,1} \times FC_{0,0} \times FC_{0,1} \times FC_{0,0} \quad (5.2)$$

Discussion

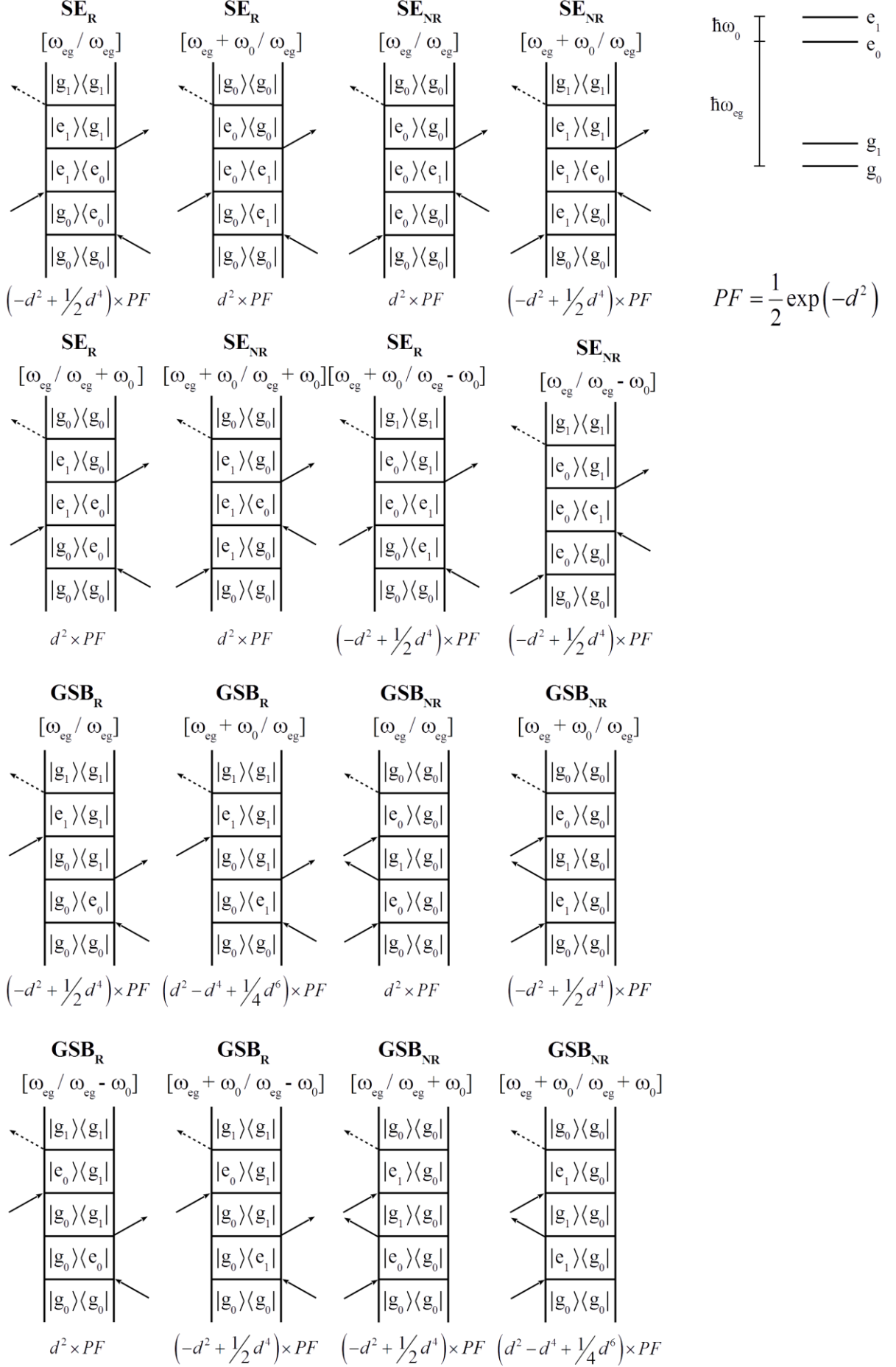
The product of the FC factors for each diagram were evaluated in Wolfram Mathematica 9.0 using Eq.(2.38) and Eq.(2.39). The results are given in Figure 20 beneath each diagram.

Since the eigenfunctions of the displaced harmonic oscillator are real valued the FC factors are real valued. Therefore the phase associated with the transition dipole product is reduced to a positive or negative sign, referring to an oscillatory phase of zero (positive sign) or π (negative sign). [41] The sign with respect to d^2 of the transition dipole products of the diagrams in Figure 20 are given in Figure 21 in a schematic 2D-ES map. The corresponding oscillatory part of the PP or Het-TG spectrum is calculated by summing up all oscillatory pathways along the ω_I – axis. Up to the second power of d and within the impulsive limit this can be done by line wise summation of the signs in Figure 21. Having done so, we can discuss the expected oscillatory amplitude and phase at the positions $\omega_3 = \omega_{eg} - \omega_0$, $\omega_3 = \omega_{eg}$ and $\omega_3 = \omega_{eg} + \omega_0$.

figure next page →

Figure 20. Summary of all double sided Feynman diagrams (excluding ESA) with vibrational coherence in t_2 for a two electronic level two vibrational level system (top right). Subscript R (NR) denotes rephasing (non rephasing) pathways. In angular brackets the position ω_I / ω_3 of the corresponding signal in a 2D-ES - spectrum is given (Stokes shift and line shapes neglected). Beneath each diagram the product of the four Franck – Condon factors involved in the diagram is given. *PF* ... pre - factor

Discussion



Discussion

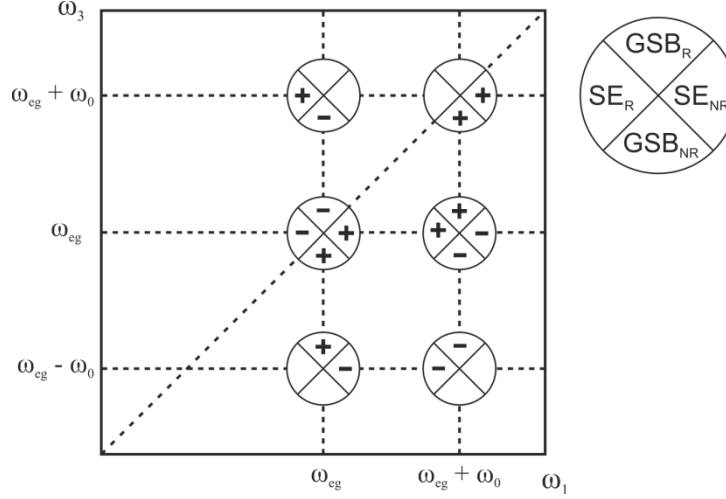


Figure 21. Spectral positions of the signals referring to the diagrams depicted in Figure 20 and their signs with respect to d^2 . The four quadrants indicate the kind of pathway and do not refer to different spectral positions. Blank quadrants indicate that no VC signal is expected. See text for interpretation.

For the electronic resonance frequency, $\omega_3 = \omega_{eg}$, we find for every diagram contributing at $\omega_1 = \omega_{eg}$ an oppositely signed diagram of the same pathway (SE_R , SE_{NR} , GSB_R , GSB_{NR}) at $\omega_1 = \omega_{eg} + \omega_0$. Therefore the signals interfere destructively up to d^2 and the experimentally found dip in amplitude is readily explained. We point out that a dip in amplitude is found for each of the four pathways individually. The finding is therefore independent of interferences between the different pathways and their relative amplitudes or phases.

At the high and low energy positions of the vibronic progression ($\omega_3 = \omega_{eg} \pm \omega_0$) the situation is different for SE and GSB contributions. For SE, a single rephasing and a single non-rephasing diagram contribute with equal sign at different positions in ω_1 . Therefore maxima of vibrational amplitude are expected at these positions, in agreement with experimental findings. The phase is expected to be π at $\omega_3 = \omega_{eg} - \omega_0$ and zero at $\omega_3 = \omega_{eg} + \omega_0$. Although the absolute values slightly deviate, the difference of π between the two sides is well represented in the data. Two rephasing GSB signals with opposing sign are expected at $\omega_3 = \omega_{eg} - \omega_0$, resulting in cancellation in ω_1 -integrated spectra. The same is true for non-rephasing GSB signals at $\omega_3 = \omega_{eg} + \omega_0$. It is therefore expected that, in the impulsive excitation limit, SE contributes more strongly to oscillatory signals at the spectral positions of vibronic progression $\omega_3 = \omega_{eg} \pm \omega_0$.

It can be shown (see Appendix C), that within the impulsive limit ($t_I = 0$) no ground state VC can be created, *i.e.* no GSB pathways can yield oscillatory signals in ω_1 -integrated spectra. This prediction, however, contradicts experimental findings, where the impulsive limit is hardly ever met. [61] It is therefore necessary to discuss the constraints of the impulsive limit and the effects of finite pulses.

Discussion

In conclusion, the methodology presented in this section could explain qualitatively the experimentally found amplitude- and phase spectra by drawing double sided Feynman diagrams and calculating the product of four FC factors for each diagram. This procedure is not only straight forward, but also applicable to a wide range of experiments in which similar vibronic coupling or coupling to phonons is observed in nonlinear optical spectra. Note, the analysis presented here is by no means limited to only two vibrational eigenstates and can be extended without adaptation. Also, the limitation to SE and GSB pathways is no principal limitation of this analysis. ESA pathways can be included in a straight forward manner by adding a third displaced potential energy surface to the system and drawing the relevant diagrams. The additional negative sign associated with ESA pathways has to be taken into account for direct comparison with SE and GSB. ESA contributions are not discussed because they are not observed in the spectra presented above. Generally, ESA in perylenes (hypericin is a phananthroperylene quinone) is far red shifted from the $S_0 \rightarrow S_1$ transition. [62,69] In a theoretical treatment, BUTKUS *et al.* found that the inclusion of ESA pathways leads to a reduction of VC-signal strength while retaining the overall phase relations between the pathways. [75]

5.3.2 Non-impulsive excitation

Up to this point we argued within the impulsive limit, *i.e.* convolution of the response function with the excitation pulses' E -field (compare Eq.(2.16)) did not influence the measured signals. This limit does not hold for the high frequency vibrational mode, since the temporal FWHM of the excitation pulses as determined from the FROG trace (~ 15 fs) is bigger than half the period of this mode (25 fs), which allows for the nuclear wavefunctions to significantly evolve in t_I during excitation. In the literature, effects of the excitation pulses on VC on the electronic ground – and excited state are well documented as they can provide a tool to selectively measure ground – or excited state VC. [71,76–79] A clear separation of these is desired as only excited state VC can play a role in processes originating from an electronic excited state.

It was demonstrated numerically [71] that the pulse duration of a transform limited pulse strongly effects the vibrational amplitude measured in pump probe and that an optimal pulse duration can be found. This is also found in Appendix C, where the effects of finite pulse durations are investigated in the frequency domain. In Appendix C and in the following discussion each transition $|1\rangle \rightarrow |2\rangle$ in a diagram is assumed to scale with the electric field amplitude $E(\omega_{1,2})$ resonant with that transition. Since finite pulse durations imply finite pulse spectra, the amplitudes $E(\omega_{eg} + \Delta\nu\omega_0)$ differ for different changes in vibrational quantum number $\Delta\nu$. The diagrams in Figure 20 include different $\Delta\nu$, so finite spectra have to be taken into account when summing up the diagrams.

A more frequently addressed cause of deviations from the findings made in the impulsive limit are chirped pulses (see Figure 10 for an assessment of the chirp in the experiments presented above). [76–79] Especially GSB contributions, *i.e.* signals from VC on the electronic ground state, are strongly affected by chirp. It was demonstrated experimentally and numerically [76] that positive chirp (red

Discussion

before blue) discriminates against ground state vibrational coherences in pump probe signals, while negative chirp (blue before red) significantly enhances them. This phenomenon was explained via the excited state wave packet created upon interaction with the blue spectral end of the pulse having time during t_1 to move on the potential energy surface to a position of greater overlap with vibrationally excited states on the electronic ground state. Therefore, upon de-excitation resonant with the red spectral end of the pulse, the wavepacket is prepared on the electronic ground state in a non-equilibrium position. This also explains the finding of WAND *et.al.* [78] that the chirp optimal for creation of ground state vibrational coherence depends on the curve displacement d . CHRISTENSSON *et.al.* [79] investigated the effect of chirped pulses on 2D-ES and found that even moderate chirp can produce significant artefacts, especially in systems with strongly coupled vibrational and electronic modes (large curve displacement d). They also found that chirped pulses can cause imaginary parts of the molecular response function to contribute to the real part of the third order polarization, *i.e.* a mixing of dispersive and absorptive contributions is observed (see section 5.3.3).

In the response function formalism, negative chirp can be considered to lead to stronger signals from diagrams in which a low energy transition is followed some time t_1 after a high energy transition and vice versa for positive chirp. Such selectivity would also lift the cancellation of pathways at $\omega_3 = \omega_{eg}$.

So far discussed effects associated with finite, real pulses become more pronounced as the vibrational mode's frequency ω_0 increases. This explains why good agreement with the predictions above could be found for the 300 cm^{-1} - and 440 cm^{-1} mode, while the 1290 cm^{-1} mode deviates significantly from the theoretical predictions. Additionally, as can be seen from Figure 18, the 1290 cm^{-1} mode overlaps with neighbouring modes and possibly additional, non-resolved modes, which likely obscures the behaviour of the "pure", isolated mode. The pronounced slope in the phase of the 1290 cm^{-1} mode is most likely attributed to chirp.

5.3.3 Finite line-widths, vibrational coherence in absolute and dispersive TG signals

So far we considered the molecular response to be limited to six precise positions in the 2D-ES plot and thereby neglected all mechanisms leading to finite line-width. By doing so we also neglected dispersive signal contributions. Fitting of the absorption spectrum (Figure 14, Table 1) yielded a FWHM of the peaks of approximately 430 cm^{-1} . Especially for the low energy vibrations significant overlap of peaks is therefore expected and has to be taken into account. Since the overlapping oscillatory signals are out of phase an increasingly pronounced dip at the central spectral position is expected for increasingly overlapping peaks. In fact the dip is found to be more pronounced for the 300 cm^{-1} - than for the 440 cm^{-1} mode.

Dispersive signals are hardly discussed in literature and no discussion of VC in dispersive signals could be found. As only absorptive signals allow for the direct simultaneous study of vibrational coherent motion and electronic population dynamics it is essential to eliminate dispersive signal contributions that would otherwise significantly obscure absorptive VC signals.

Discussion

We give a brief general discussion of possible influences of dispersive oscillatory signals on vibrational signals as measured via unphased, absolute TG or inadequately phased Het-TG or other FWM techniques, such as 2D-ES. Although absorptive and dispersive signals are orthogonal (*i.e.* non-interfering) in t_3 (they are defined by their phase difference of $\pi/2$), their oscillations in t_2 do interfere. It is important to notice that the vibrational amplitude in absolute TG as presented in Figure 19 is not simply given by the sum of amplitudes in real (absorptive) and imaginary (dispersive) TG, but by the sum of two complex amplitudes A_C .

$$A_{C,abs} = A_{abs}, \varphi_{abs} = \varphi_{C,real} + \varphi_{C,im} \quad (5.3)$$

$$A_{abs} = \sqrt{A_{real}^2 + A_{im}^2 - 2A_{real}A_{im}\cos(\pi - \Delta\varphi)} \quad (5.4)$$

$$\varphi_{abs} = \arctan\left(\frac{A_{im}\sin(\varphi_{im}) + A_{real}\sin(\varphi_{real})}{A_{real}\cos(\varphi_{real}) + A_{im}\sin(\varphi_{im})}\right) \quad (5.5)$$

Herein, subscripts *abs* / *real* / *im* denote vibrational amplitudes A and phases φ measured in absolute / real (absorptive) / imaginary (dispersive) TG or 2D-ES. $\Delta\varphi$ is the difference in phase between oscillations in real and imaginary signals. The complex summation explains why vibrational amplitudes in absolute TG are found to be smaller than in real TG at some positions but bigger at others.

6 Conclusion

Femtosecond nonlinear transient grating spectra of hypericin were shown to resolve molecular vibrational motion in the time domain. This method was chosen carefully, after establishing that pump-probe spectroscopy yields a lower signal to noise ratio and 2D electronic spectroscopy suffers under too long data acquisition times. The vibrations' amplitude and phase were plotted as a function of detection wavelength (Figure 19). To extract these values from the time resolved spectra a new method was developed based on a global fitting routine. Evaluation of the method proved its reliability and showed that errors in alternative methods such as discrete Fourier transformation, linked to the discrete sampling of frequencies, can be avoided by making the frequency a continuous fitting parameter.

Vibrational amplitude and phase spectra were compared to theoretical predictions derived for a displaced harmonic oscillator. Theoretical analysis was based on response theory of optical spectroscopy which was discussed in chapter 2 starting from a density matrix description of the molecule and arriving at double sided Feynman diagrams. To compare the diagrams contributing to different positions in the spectra, the four transition dipole moments scaling each diagram were analysed. By invoking the Franck-Condon principle, the transition dipole moments were weighted by their specific Franck-Condon factors. It was found that, due to opposing signs of the products of the four Franck-Condon factors, some diagrams cancel each other at one position in the spectrum and constructively overlap at others. The sign of the Franck-Condon factor also reflected the experimentally found phase of the vibrational signals.

Agreement between experiment and theory was found for vibrational modes of 300 cm^{-1} and 440 cm^{-1} in the phased absorptive transient grating spectrum. Vibrational spectra of unphased data deviate significantly from their phased counterparts, which is readily explained by mixing of dispersive and absorptive signals. Additionally, the spectra of hypericin's 1290 cm^{-1} mode were found to contradict theoretical predictions. Effects from finite laser pulse spectra and the pulses' chirp were discussed and shown to be more severe for higher frequency vibrations, explaining the experimental differences between high and low frequency modes.

In summary, we showed that vibrational dynamics in both phase and amplitude is readily explained in the response function formalism, extended by transition specific Franck-Condon factors. This analytical treatment gives a physical and comprehensive picture of all phenomena observed in vibronic spectra of hypericin and is a fully equivalent alternative to the computationally more demanding wavepacket formalism.

Appendix

Appendix

Appendix A. Calculation of the first order polarization of a two level system

In an effort to demonstrate the role of transition dipole moments in optical signals of different order we calculate

$$P^{(1)}(t) = \text{Tr}(\mu \rho^{(1)}(t)) \quad (\text{A.1})$$

for

$$\rho_{eq} = |0\rangle\langle 0|, \quad (\text{A.2})$$

i.e. we assume no thermal population of excited states. Eq.(2.12) then reads

$$\begin{aligned} \rho_{nm}^{(1)}(t) &= \frac{i}{\hbar} \int_{-\infty}^t d\tau_0 \exp(-i\omega_{nm}(t-\tau_0)) E(\tau_0) [\mu, \rho_{eq}]_{nm} \\ &= \frac{i}{\hbar} \int_{-\infty}^t d\tau_0 J_{nm}(t-\tau_0) E(\tau_0) \times (\delta_{0m}\mu_{n0} - \delta_{0n}\mu_{0m}) \end{aligned} \quad (\text{A.3})$$

Herein, we made use of Eq.(A.4) - (A.6) as well as Eq.(2.23) (compare Eq.(2.4) and Eq.(A.2)).

$$[\mu, \rho_{eq}(\tau_0)]_{01} = \langle n | (\mu | 0\rangle\langle 0| - |0\rangle\langle 0| \mu) | m \rangle = \langle n | \mu | 0\rangle\langle 0 | m \rangle - \langle n | 0\rangle\langle 0 | \mu | m \rangle = \delta_{0m}\mu_{n0} - \delta_{0n}\mu_{0m} \quad (\text{A.4})$$

$$\langle n | m \rangle = \delta_{nm} \quad (\text{A.5})$$

$$\langle n | \mu | m \rangle = \mu_{nm} \quad (\text{A.6})$$

Herein, δ_{nm} is the Kronecker delta function. Eq.(A.5) states that we assume an orthonormal basis of eigenfunctions.

If we now turn to a two level system constituted of the eigenkets $|0\rangle$ and $|1\rangle$, ρ_{eq} takes the form

$$\rho_{eq} = |0\rangle\langle 0| = \begin{pmatrix} 1 & 0 \\ 0 & 0 \end{pmatrix}. \quad (\text{A.7})$$

Eq.(A.3) can then be used to calculate the elements of $\rho^{(1)}(t)$:

$$\rho_{01}^{(1)}(t) = \frac{i}{\hbar} \int_{-\infty}^t d\tau_0 J_{01}(t-\tau_0) E(\tau_0) \times (-\mu_{01}(\tau_0)) \quad (\text{A.8})$$

$$\rho_{10}^{(1)}(t) = \frac{i}{\hbar} \int_{-\infty}^t d\tau_0 J_{10}(t-\tau_0) E(\tau_0) \times \mu_{10}(\tau_0) \quad (\text{A.9})$$

$$\rho_{00}^{(1)}(t) = \frac{i}{\hbar} \int_{-\infty}^t d\tau_0 J_{00}(t-\tau_0) E(\tau_0) \times (\mu_{00}(\tau_0) - \mu_{00}(\tau_0)) = 0 \quad (\text{A.10})$$

$$\rho_{11}^{(1)}(t) = \frac{i}{\hbar} \int_{-\infty}^t d\tau_0 J_{11}(t-\tau_0) E(\tau_0) \times 0 = 0 \quad (\text{A.11})$$

Appendix

Inserting Eq.(A.8) - (A.11) into Eq.(A.1) we write

$$P^{(1)}(t) = \text{Tr}(\mu \rho^{(1)}(t)) = [\mu \rho^{(1)}(t)]_{00} + [\mu \rho^{(1)}(t)]_{11} \quad (\text{A.12})$$

$$\rho^{(1)} = \sum_{nm} \rho_{nm}^{(1)} |n\rangle \langle m| \quad (\text{A.13})$$

$$[\mu \rho^{(1)}]_{00} = \langle 0 | \mu \rho^{(1)} | 0 \rangle = \sum_{nm} \rho_{nm}^{(1)} \langle 0 | \mu | n \rangle \langle m | 0 \rangle = \rho_{10}^{(1)}(t) \mu_{01} \quad (\text{A.14})$$

$$[\mu \rho^{(1)}]_{11} = \langle 1 | \mu \rho^{(1)} | 1 \rangle = \sum_{nm} \rho_{nm}^{(1)} \langle 1 | \mu | n \rangle \langle m | 1 \rangle = \rho_{01}^{(1)}(t) \mu_{10} \quad (\text{A.15})$$

to arrive at

$$P^{(1)}(t) = \frac{i}{\hbar} \left(\mu_{01} \int_{-\infty}^t d\tau_0 J_{10}(t - \tau_0) E(\tau_0) \times \mu_{10} + \mu_{10} \int_{-\infty}^t d\tau_0 J_{01}(t - \tau_0) E(\tau_0) \times (-\mu_{01}) \right). \quad (\text{A.16})$$

Since $\mu_{01}\mu_{10} = |\mu_{10}|^2 = |\mu_{01}|^2$ we can rewrite Eq.(A.16) as

$$P^{(1)}(t) = \frac{i}{\hbar} |\mu_{10}|^2 \int_{-\infty}^t d\tau_0 E(\tau_0) (J_{10}(t - \tau_0) - J_{01}(t - \tau_0)) = \frac{i}{\hbar} \int_{-\infty}^t d\tau_0 E(\tau_0) S^{(1)}(t, \tau_0). \quad (\text{A.17})$$

When writing out the auxiliary functions Eq.(2.23) the response function $S^{(1)}(t, \tau_0)$ takes the form

$$S^{(1)}(t, \tau_0) = |\mu_{10}|^2 \left(\exp(-i\omega_{10}(t - \tau_0)) - \exp(i\omega_{10}(t - \tau_0)) \right). \quad (\text{A.18})$$

More generally, for a molecular system with an arbitrary number of eigenstates and thermal population of states other than the ground state, $S^{(1)}(t, \tau_0)$ reads (see REZUS [23], Eq.(2.25))

$$S^{(1)}(t, \tau_0) = \sum_{ab} J_{ba}(t - \tau_0) |\mu_{ba}|^2 \rho_{eq,aa} - \sum_{ab} J_{ab}(t - \tau_0) |\mu_{ba}|^2 \rho_{eq,aa}. \quad (\text{A.19})$$

Appendix B. Evaluation of time domain GA for the retrieval of oscillatory phase- and amplitude spectra

Evaluation of the GA method of retrieving oscillatory phases and amplitudes in the time domain was performed by creating test data and analyzing it *via* GA and FFT. The test data was calculated as a sum of five exponentially decaying oscillations

$$E_{test}(t_2, \omega_3) = wgn + \sum_{i=1 \dots 5} A(\omega_3) \times \exp(-t_2/\tau_i) \times \cos(\omega_i \times (t_2 + \Delta t) + \varphi_i(\omega_3)), \quad (\text{A.20})$$

sampled on the same grid used for the experimental Het-TG data presented in Figure 17. Herein, *wgn* stands for white Gaussian noise added to the data to give an overall signal to noise ratio (SNR) of 0.36. The SNR was defined as the ratio of integrated power of the signal and the integrated power of the noise in the ω_2 domain. From experimental data a value of SNR = 0.36 was estimated. Δt is a Gaussian distributed phase instability. For a comparative FFT analysis the data was eight-fold zero

Appendix

padding to 4096 datapoints. The amplitude - and phase spectra were extracted by slicing through the Fourier transformed data at the desired value of ω_2 and calculating the absolute value and phase of the complex Fourier amplitude. The found amplitude – and phase spectra of both GA and FFT were smoothened *via* a Savitzky Golay filter. The spectra were compared to the input spectra by calculating the Pearson correlation coefficient of the input – and output spectra.

The GA fitting routine was found to converge to the same results for initial frequency parameters varying by two percent of the true frequencies ω_i and a factor of two around the true decay-rates τ_i . GA also converged for noise corresponding to a SNR of 0.1 and additional phase instability Δt of 1 fs. The results for a dataset calculated using the parameters defined in Table A1 are presented in Figure A1. The Pearson correlation coefficients of the spectra and the input spectra as well as frequencies ω_i and decay constants τ_i found via GA are given in Table A2.

Table A1. Model parameters for the dataset analyzed in Figure A1.

						SNR	Δt FWHM / fs
Frequency ω_i / cm^{-1}	290	450	1200	1280	1367	0.36	0.2
Decay constant τ_i / ps	0,577	0,433	0,245	0,433	0,721		

Table A2. Results of GA and FFT analysis. R^2 for the 1200 cm^{-1} cannot be calculated because the input phase is a constant value.

Mode / cm^{-1}	290	450	1200	1280	1367
$R^2(A_{\text{GA}}(\omega_3))$	0.956	0.986	0.989	0.987	0.949
$R^2(A_{\text{FFT}}(\omega_3))$	0.972	0.988	0.952	0.936	0.935
$R^2(\varphi_{\text{GA}}(\omega_3))$	0.996	0.998	-	0.995	0.994
$R^2(\varphi_{\text{FFT}}(\omega_3))$	0.996	0.996	-	0.806	0.987
GA fit for ω_i / cm^{-1}	290.0	449.9	1197.2	1281.4	1367.5
GA fit for τ_i / ps	0.643	0.459	0.284	0.480	0.805

Both, FFT analysis and GA could reconstruct the basic shape of the amplitude spectra and yielded Pearson R^2 factors well above 0.93. In the reconstruction of the phase spectra the time domain GA routine outperformed the studied FFT routine. Firstly, the correlation coefficient is higher for all modes and the spectra appear in general less noisy. Secondly, the time domain method not only reconstructed the shape of the phase spectrum but yielded the correct absolute values. The FFT – method suffers from the steep phase jump along the frequency axis ω_2 that appears at the transition frequency in the FFT – spectrum (see Figure 3). Since the frequency axis is discrete, the “true” frequency is not sampled. This results in significant errors in the phase calculated from the real part and the rapidly changing imaginary part of the FFT – amplitude.

Appendix

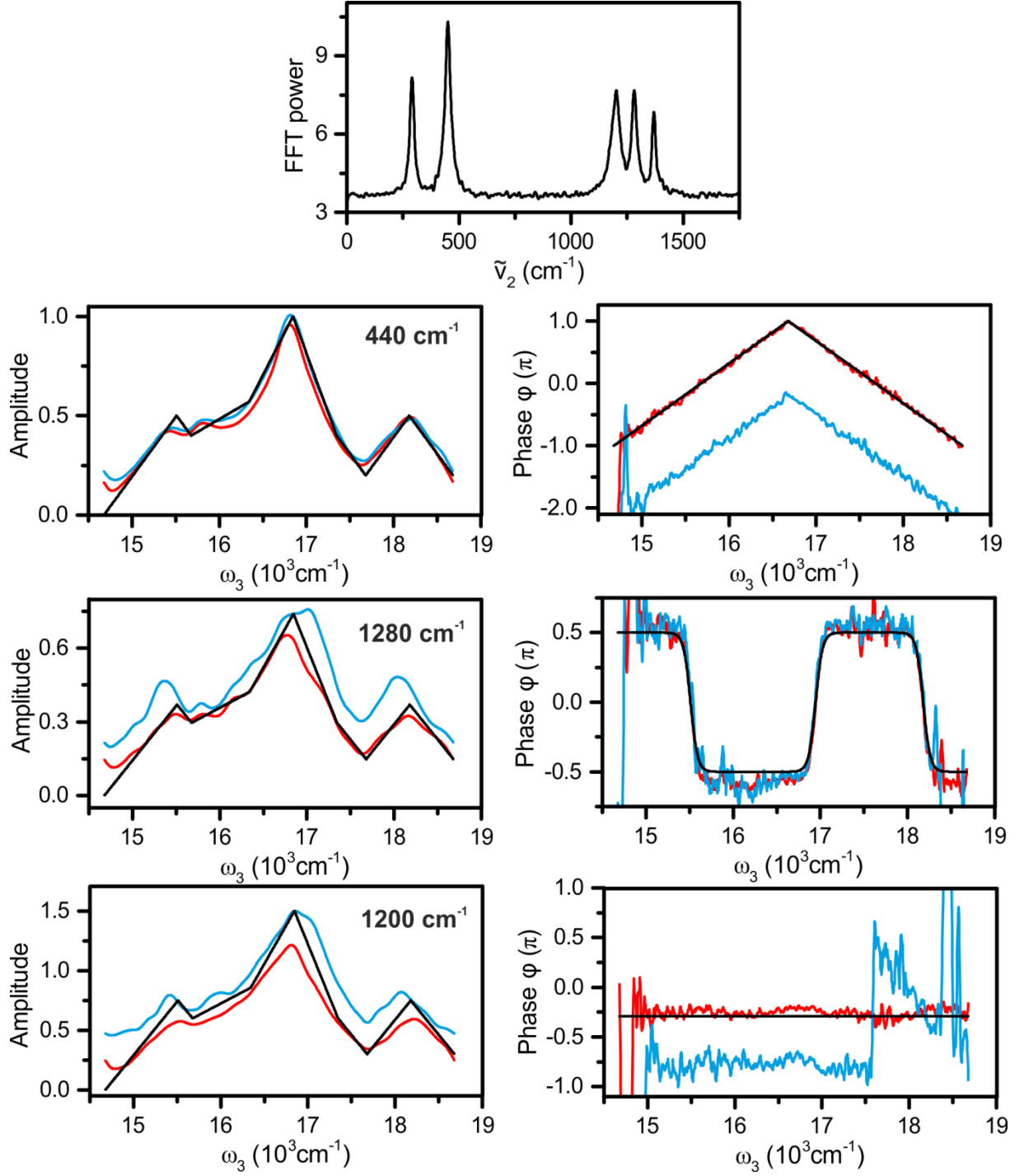


Figure A1. Evaluation of methods for amplitude- and phase- retrieval from oscillations recorded in the time domain. Top: FFT power – spectrum of the input dataset projected onto the ω_2 – axis. Left: Amplitude spectra of the indicated oscillations. Right: Phase spectra corresponding to the left hand amplitude spectra. Black lines correspond to input (ideal), red lines to results found via GA and blue lines to results found via FFT. Amplitude spectra from FFT analysis were normalized to the amplitude at 16844 cm^{-1} . All other results are presented as calculated.

Appendix C. Ground state vibrational coherence and the impulsive limit

To demonstrate that, in the impulsive limit, no ground state vibrational coherence can be observed in ω_I -integrated spectroscopic techniques (PP, TG) we calculate the ground state elements $\rho_{n0}^{(2)} = \langle g_n | \rho^{(2)} | g_0 \rangle$ of the second order density matrix $\rho^{(2)}$ after two simultaneous dipole interactions. These density matrix elements or there c.c. participate in all third order VC diagrams of GSB pathways (in the diagrams, $\rho_{n0}^{(2)}$ is represented by $|g_n\rangle\langle g_0|$). Therefore the matrix elements can be taken as a measure for the amplitude of the corresponding signals. We follow the procedure outlined in section 5.3.1, but include a larger number of vibrational eigenstates. In equilibrium, $\rho_{eq,00}$ is considered to be 1, all others 0. As illustrated in Figure A2 **b**, the second order density matrix element $\rho_{n0}^{(2)}$ can be reached via a number of trajectories $\rho_{eq,00} \rightarrow \langle e_m | \rho^{(1)} | g_0 \rangle \rightarrow \rho_{n0}^{(2)}$. Each trajectory scales with two FC factors, $FC_{0,m} FC_{n,m}$. $\rho_{n0}^{(2)}$ scales with the sum over all trajectories with appropriate sign.

$$\rho_{n0}^{(2)} \sim \sum_m FC_{0,m} FC_{n,m} \quad (\text{A.21})$$

The sum in Eq.(A.21) was evaluated in Mathematica 9.0 for the wave functions described by Eq.(2.39) for $m = 0 \dots 20$ using analytical formulas for $FC_{n,m}$ reported by CHANG [80]. Independent of the displacement d , the sum was found to vanish for all elements $\rho_{n0}^{(2)}$ except for $\rho_{00}^{(2)}$, proofing that no ground state vibrational coherences can be created impulsively.

In an attempt to investigate the boundaries of the impulsive limit in the simplest possible way we modify Eq.(A.21) by assuming that every transition scales with the electric field amplitude $E(\omega_{1,2})$ resonant with the transition $|1\rangle \rightarrow |2\rangle$:

$$\rho_{n0}^{(2)} = \sum_m E(\omega_{eg} + m\omega_0) FC_{0,m} \times E(\omega_{eg} + (m-n)\omega_0) FC_{n,m} \quad (\text{A.22})$$

$\rho_{n0}^{(2)}$ is plotted in Figure A2 for $n = 0 \dots 3$ as a function of temporal pulse length in units of vibrational period. The electric field amplitude was modeled by a Gaussian profile. Note that, for $n = 0$, $1 - \rho_{00}^{(2)}$ is plotted.

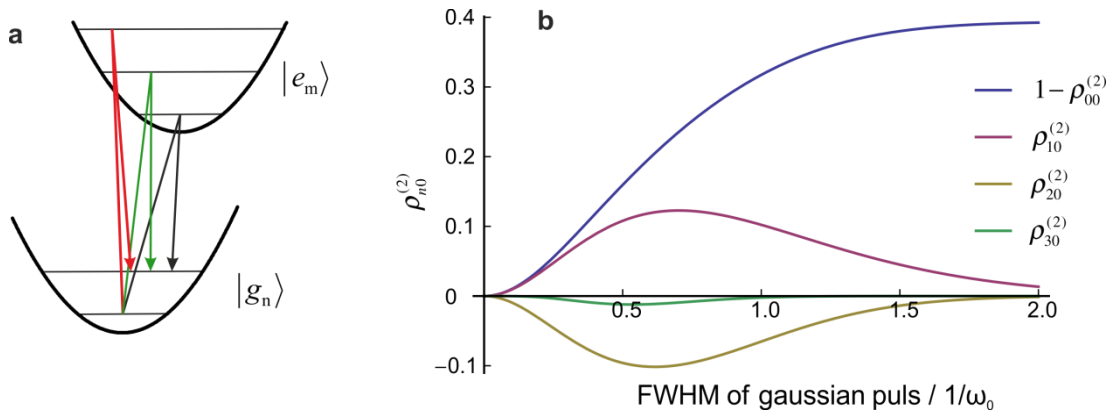


Figure A2. **a**: Trajectories leading to $\rho_{n0}^{(2)}$. **b**: $\rho_{n0}^{(2)}$ as a function of pulse duration for a curve displacement $d = 1$.

References

1. S. Ruetzel, M. Diekmann, P. Nuernberger, C. Walter, B. Engels, and T. Brixner, "Multidimensional spectroscopy of photoreactivity.," *Proc. Natl. Acad. Sci. U. S. A.* **111**, 4764–9 (2014).
2. S. Pedersen, L. Bañares, and A. H. Zewail, "Femtosecond vibrational transition-state dynamics in a chemical reaction," *J. Chem. Phys.* **97**, 8801 (1992).
3. M. Volkhard and K. Oliver, *Charge and Energy Transfer Dynamics in Molecular Systems, 3rd, Revised and Enlarged Edition* (Wiley-VCH, 2011).
4. S. Lochbrunner, A. J. Wurzer, and E. Riedle, "Microscopic Mechanism of Ultrafast Excited-State Intramolecular Proton Transfer : A 30-fs," 10580–10590 (2003).
5. J. Kim, W. Heo, and T. Joo, "Excited State Intramolecular Proton Transfer Dynamics of 1-Hydroxy-2-acetonaphthone.," *J. Phys. Chem. B* **119**, 2620–7 (2015).
6. J. Lim, D. Paleček, F. Caycedo-Soler, C. N. Lincoln, J. Prior, H. von Berlepsch, S. F. Huelga, M. B. Plenio, D. Zigmantas, and J. Hauer, "Vibronic origin of long-lived coherence in an artificial molecular light harvester.," *Nat. Commun.* **6**, 7755 (2015).
7. V. Perlík, J. Seibt, L. J. Cranston, R. J. Cogdell, C. N. Lincoln, J. Savolainen, F. Šanda, T. Mančal, and J. Hauer, "Vibronic coupling explains the ultrafast carotenoid-to-bacteriochlorophyll energy transfer in natural and artificial light harvesters.," *J. Chem. Phys.* **142**, 212434 (2015).
8. R. Berera, R. van Grondelle, and J. T. M. Kennis, "Ultrafast transient absorption spectroscopy: principles and application to photosynthetic systems.," *Photosynth. Res.* **101**, 105–18 (2009).
9. A. Mokhtari, P. Cong, J. L. Herek, and A. H. Zewail, "Direct femtosecond mapping of trajectories in a chemical reaction," *Nature* **348**, 225–227 (1990).
10. A. H. Zewail, "Femtochemistry: Atomic-scale dynamics of the chemical bond," *J. Phys. Chem. A* **104**, 5660–5694 (2000).
11. E. Vauthey, "Introduction to nonlinear optical spectroscopic techniques for investigating ultrafast processes," 1–40 (2006).
12. S. Mukamel, *Principles of Nonlinear Optical Spectroscopy* (Oxford University Press, USA, 1995).
13. M. Motzkus, S. Pedersen, and A. H. Zewail, "Femtosecond real-time probing of reactions .19. Nonlinear (DFWM) techniques for probing transition states of uni- and bimolecular reactions," *J. Phys. Chem.* **100**, 5620–5633 (1996).
14. a M. Zheltikov, "Coherent anti-Stokes Raman scattering: from proof-of-the-principle experiments to femtosecond CARS and higher order wave-mixing generalizations," *J. Raman Spectrosc.* **31**, 653–667 (2000).
15. G. Herzberg, *Molecular Spectra and Molecular Structure. 3. Electronic Spectra and Electronic Structure of Polyatomic Molecules* (Van Nostrand, 1967).
16. J. Franck and E. G. Dymond, "Elementary processes of photochemical reactions," *Trans. Faraday Soc.* **21**, 536 (1926).
17. E. Condon, "A Theory of Intensity Distribution in Band Systems," *Phys. Rev.* **28**, 1182–1201 (1926).
18. J. Hauer, T. Buckup, and M. Motzkus, "Pump-degenerate four wave mixing as a technique for analyzing structural and electronic evolution: Multidimensional time-resolved dynamics near a conical intersection," *J. Phys. Chem. A* **111**, 10517–10529 (2007).
19. H. Falk, "From the Photosensitizer Hypericin to the Photoreceptor StentorinÐ The Chemistry of Phenanthroperylene Quinones," (n.d.).
20. D. Meruelo, G. Lavie, and D. Lavie, "Therapeutic agents with dramatic antiretroviral activity and little toxicity at effective doses: aromatic polycyclic diones hypericin and pseudohypericin.," *Proc. Natl. Acad. Sci. U. S. A.* **85**, 5230–4 (1988).
21. M. J. F. M. A. McCloskey and J. W. Petrich, "Light-Induced Acidification by the Antiviral Agent Hypericin," 1833–1836 (1995).
22. F. Sureau, P. Miskovsky, L. Chinsky, P. Y. Turpin, P. M. Curie, P. Jussieu, P. Cedex, B. Di V, S. U. V, V. Slo, and R. V May, "Hypericin-Induced Cell Photosensitization Involves an

Appendix

- Intracellular pH Decrease," **7863**, 9484–9487 (1996).
23. Y. Rezus, "Snapshots of water: Orientational dynamics of hydrogen-bonded systems," Foundation for Fundamental Research on Matter (2008).
24. A. Tokmakoff, "Time-Dependent Quantum Mechanics and Spectroscopy," <http://tdqms.uchicago.edu/>.
25. R. Littlejohn, "Mathematical Formalism of Quantum mechanics," <http://bohr.physics.berkeley.edu/classes/221/1112/notes/hilbert.pdf>.
26. P. A. M. Dirac, *The Principles of Quantum Mechanics* (Clarendon Press, 1981).
27. S. Mukamel and D. Abramavicius, "Many-body approaches for simulating coherent nonlinear spectroscopies of electronic and vibrational excitons," *Chem. Rev.* **104**, 2073–2098 (2004).
28. R. W. Boyd, "Molecular Origin of the Nonlinear Optical Response," in *Nonlinear Optics* (Elsevier, 2008), pp. 253–275.
29. P. Hamm and M. Zanni, *Concepts and Methods of 2D Infrared Spectroscopy* (Cambridge University Press, 2011).
30. R. W. Boyd, "Wave-Equation Description of Nonlinear Optical Interactions," in *Nonlinear Optics*, 3rd ed. (Elsevier, 2008), pp. 69–133.
31. E. Hahn, "Spin Echoes," *Phys. Rev.* **80**, 580–594 (1950).
32. M. Kozłowski, S. Garrett-Roe, and P. Hamm, "Vibrational spectral diffusion of CN[−] in water," *Chem. Phys.* **341**, 5–10 (2007).
33. F. Sanda, V. Perlik, C. N. Lincoln, and J. Hauer, "Center Line Slope Analysis in Two-Dimensional Electronic Spectroscopy," *J. Phys. Chem. A* (2015).
34. S. T. Roberts, J. J. Loparo, and A. Tokmakoff, "Characterization of spectral diffusion from two-dimensional line shapes," *J. Chem. Phys.* **125**, 084502 (2006).
35. D. M. Jonas, "Two - Dimensional Femtosecond Spectroscopy," *Annu. Rev. Phys. Chem.* **54**, 425–463 (2003).
36. N. Christensson, F. Milota, A. Nemeth, J. Sperling, H. F. Kauffmann, T. Pullerits, and J. Hauer, "Two-dimensional electronic spectroscopy of beta-carotene," *J. Phys. Chem. B* **113**, 16409–16419 (2009).
37. M. Khalil, N. Demirdöven, and A. Tokmakoff, "Obtaining Absorptive Line Shapes in Two-Dimensional Infrared Vibrational Correlation Spectra," *Phys. Rev. Lett.* **90**, 047401 (2003).
38. G. A. Reider, *Photonik - Eine Einführung in Die Grundlagen*, 3rd ed. (Springer, 2012).
39. G. Herzberg, *Molecular Spectra and Molecular Structure. 1. Spectra of Diatomic Molecules*, 2nd ed. (Van Nostrand, 1966).
40. G. Herzberg, *Molecular Spectra and Molecular Structure. 2. Infrared and Raman Spectra of Polyatomic Molecules* (Van Nostrand, 1966).
41. D. a. Farrow, E. R. Smith, W. Qian, and D. M. Jonas, "The polarization anisotropy of vibrational quantum beats in resonant pump-probe experiments: Diagrammatic calculations for square symmetric molecules," *J. Chem. Phys.* **129**, (2008).
42. G. Cerullo and S. De Silvestri, "Ultrafast optical parametric amplifiers," *Rev. Sci. Instrum.* **74**, 1–18 (2003).
43. J. Piel, E. Riedle, L. Gundlach, R. Ernstorfer, and R. Eichberger, "Sub-20 fs visible pulses with 750 nJ energy from a 100 kHz noncollinear optical parametric amplifier," *Opt. Lett.* **31**, 1289 (2006).
44. J.-C. Diels and W. Rudolph, "Ultrashort Sources I: Fundamentals," in *Ultrashort Laser Pulse Phenomena* (Elsevier, 2006), pp. 277–339.
45. J.-C. Diels and W. Rudolph, "Ultrashort Sources II: Examples," in *Ultrashort Laser Pulse Phenomena* (Elsevier, 2006), pp. 341–394.
46. J.-C. Diels and W. Rudolph, "Femtosecond Pulse Amplification," in *Ultrashort Laser Pulse Phenomena* (Elsevier, 2006), pp. 395–431.
47. J.-C. Diels and W. Rudolph, "Pulse Shaping," in *Ultrashort Laser Pulse Phenomena* (Elsevier, 2006), pp. 433–456.
48. A. M. Weiner, "Ultrafast optical pulse shaping: A tutorial review," *Opt. Commun.* **284**, 3669–3692 (2011).
49. R. L. Fork, O. E. Martinez, and J. P. Gordon, "Negative dispersion using pairs of prisms," *Opt. Lett.* **9**, 150–152 (1984).
50. J. D. Kafka and T. Baer, "Prism-pair dispersive delay lines in optical pulse compression," *Opt.*

Appendix

- Lett. **12**, 401–403 (1987).
51. R. Trebino, K. W. DeLong, D. N. Fittinghoff, J. N. Sweetser, M. A. Krumbügel, B. A. Richman, and D. J. Kane, "Measuring ultrashort laser pulses in the time-frequency domain using frequency-resolved optical gating," *Rev. Sci. Instrum.* **68**, 3277 (1997).
 52. F. Milota, C. N. Lincoln, and J. Hauer, "Precise phasing of 2D-electronic spectra in a fully non-collinear phase-matching geometry.," *Opt. Express* **21**, 15904–11 (2013).
 53. F. D. Fuller and J. P. Ogilvie, "Experimental Implementations of Two-Dimensional Fourier Transform Electronic Spectroscopy," *Annu. Rev. Phys. Chem.* **66**, 667–690 (2015).
 54. P. Gbur, R. Dedic, D. Chorvat, P. Miskovsky, J. Hala, and D. Jancura, "Time-resolved luminescence and singlet oxygen formation after illumination of the hypericin-low-density lipoprotein complex," *Photochem. Photobiol.* **85**, 816–823 (2009).
 55. M. J. Tauber, R. A. Mathies, X. Chen, and S. E. Bradforth, "Flowing liquid sample jet for resonance Raman and ultrafast optical spectroscopy," *Rev. Sci. Instrum.* **74**, 4958 (2003).
 56. C. Didraga, A. Pugžlys, P. R. Hania, H. von Berlepsch, K. Duppen, and J. Knoester, "Structure, Spectroscopy, and Microscopic Model of Tubular Carbocyanine Dye Aggregates," *J. Phys. Chem. B* **108**, 14976–14985 (2004).
 57. J. Brazard, L. A. Bizimana, and D. B. Turner, "Accurate convergence of transient-absorption spectra using pulsed lasers," *Rev. Sci. Instrum.* **86**, 053106 (2015).
 58. R. Bracewell, "The Projection-Slice Theorem," in *Fourier Analysis and Imaging* (Springer US, 2003), pp. 493–504.
 59. I. H. M. van Stokkum, D. S. Larsen, and R. van Grondelle, "Global and target analysis of time-resolved spectra," *Biochim. Biophys. Acta - Bioenerg.* **1657**, 82–104 (2004).
 60. L. J. G. W. van Wilderen, C. N. Lincoln, and J. J. van Thor, "Modelling multi-pulse population dynamics from ultrafast spectroscopy," *PLoS One* **6**, e17373 (2011).
 61. M. Liebel, C. Schnedermann, T. Wende, and P. Kukura, "Principles and Applications of Broadband Impulsive Vibrational Spectroscopy," *J. Phys. Chem. A* 150811102907007 (2015).
 62. R. C. Guedes and L. a. Eriksson, "Theoretical study of hypericin," *J. Photochem. Photobiol. A Chem.* **172**, 293–299 (2005).
 63. M. Mylrajan, P. Hildebrandt, and Y. Mazur, "Vibrational spectroscopy of hypericin, its sodium salt and pyridinium complex," *J. Mol. Struct.* **407**, 5–10 (1997).
 64. G. D. Goodno, G. Dadusc, and R. J. D. Miller, "Ultrafast heterodyne-detected transient-grating spectroscopy using diffractive optics," *J. Opt. Soc. Am. B* **15**, 1791 (1998).
 65. I. a Heisler, R. Moca, F. V. a Camargo, and S. R. Meech, "Two-dimensional electronic spectroscopy based on conventional optics and fast dual chopper data acquisition.," *Rev. Sci. Instrum.* **85**, 063103 (2014).
 66. M. Sedlacek and M. Krumpholtz, "Digital measurement of phase difference - a comparative study of DSP algorithms," *Metrol. Meas. Syst.* **Vol. 12, n**, 427–448 (2005).
 67. R. Micheletti, "Phase angle measurement between two sinusoidal signals," *Instrum. Meas. IEEE Trans.* **40**, 40–42 (1991).
 68. W. T. Pollard, S. L. Dexheimer, Q. Wang, L. a Peteanu, C. V Shank, and R. a Mathies, "Theory of dynamic absorption spectroscopy of nonstationary states. 4. Application to 12-fs resonant impulsive Raman spectroscopy of bacteriorhodopsin," *J. Phys. Chem.* **96**, 6147–6158 (1992).
 69. M. Son, K. H. Park, M.-C. Yoon, P. Kim, and D. Kim, "Excited-State Vibrational Coherence in Perylene Bisimide Probed by Femtosecond Broadband Pump–Probe Spectroscopy," *J. Phys. Chem. A* 150602130727003 (2015).
 70. L. Lüer, C. Gadermaier, J. Crochet, T. Hertel, D. Brida, and G. Lanzani, "Coherent phonon dynamics in semiconducting carbon nanotubes: A quantitative study of electron-phonon coupling," *Phys. Rev. Lett.* **102**, 2–5 (2009).
 71. D. M. Jonas, S. E. Bradforth, S. A. Passino, and G. R. Fleming, "Femtosecond Wavepacket Spectroscopy: Influence of Temperature, Wavelength, and Pulse Duration," *J. Phys. Chem.* **99**, 2594–2608 (1995).
 72. B. M. Garraway and K.-A. Suominen, "Wave-packet dynamics: new physics and chemistry in femto-time," *Reports Prog. Phys.* **58**, 365–419 (1995).
 73. T. Mančal, N. Christensson, V. Lukeš, F. Milota, O. Bixner, H. F. Kauffmann, and J. Hauer, "System-dependent signatures of electronic and vibrational coherences in electronic two-

Appendix

- dimensional spectra," *J. Phys. Chem. Lett.* **3**, 1497–1502 (2012).
74. S. M. G. Faeder and D. M. Jonas, "Phase-resolved time-domain nonlinear optical signals," *Phys. rev. A* **62**, 33820 (2000).
75. V. Butkus, D. Zigmantas, L. Valkunas, and D. Abramavicius, "Vibrational vs. electronic coherences in 2D spectrum of molecular systems," *Chem. Phys. Lett.* **545**, 40–43 (2012).
76. C. J. Bardeen, Q. Wang, and C. V. Shank, "Femtosecond chirped pulse excitation of vibrational wave packets in LD690 and bacteriorhodopsin," *J. Phys. Chem. A* **102**, 2759–2766 (1998).
77. C. J. Bardeen, Q. Wang, and C. V. Shank, "Selective excitation of vibrational wave packet motion using chirped pulses," *Phys. Rev. Lett.* **75**, 3410–3413 (1995).
78. A. Wand, S. Kallush, O. Shoshanim, O. Bismuth, R. Kosloff, and S. Ruhman, "Chirp effects on impulsive vibrational spectroscopy: a multimode perspective," *Phys. Chem. Chem. Phys.* **12**, 2149 (2010).
79. N. Christensson, Y. Avlasevich, A. Yartsev, K. Müllen, T. Pascher, and T. Pullerits, "Weakly chirped pulses in frequency resolved coherent spectroscopy," *J. Chem. Phys.* **132**, (2010).
80. J. L. Chang, "A new formula to calculate Franck-Condon factors for displaced and distorted harmonic oscillators," *J. Mol. Spectrosc.* **232**, 102–104 (2005).